UCLA
COMPUTATIONAL AND APPLIED MATHEMATICS

Multiresolution Based on Weighted Averages of the Hat Function II: Non-Linear Reconstruction Techniques

Francesc Arandiga
Rosa Donat
Ami Harten

August 1996

CAM Report 96-26

Department of Mathematics
University of California, Los Angeles
Los Angeles, CA. 90024-1555

MULTIRESOLUTION BASED ON WEIGHTED AVERAGES OF THE HAT FUNCTION II: NON-LINEAR RECONSTRUCTION TECHNIQUES

FRANCESC ARÀNDIGA*, ROSA DONAT† AND AMI HARTEN ‡

Abstract. We continue to study the properties of the multiresolution analysis corresponding to discretization by local averages with respect to the hat function initiated in Part I [3]. In this paper we describe and analyze a class of non-linear multiresolution schemes for the hat-average multiresolution setting. These schemes are based on the Essentially-Non-Oscillatory (ENO) interpolatory procedure described in [12]. We show that by allowing the approximation to fit the local nature of the data, one can improve the compression capabilities of the multiresolution based compression algorithms. The question of stability for non-linear (data-dependent) reconstruction techniques is also addressed.

Key Words. Multiresolution, adaptive stencils, Subcell Resolution

AMS(MOS) subject classifications. 41A05, 41A15, 65015

* Departament de Matemàtica Aplicada. Universitat de València (Spain). Research supported in part by by DGICYT PB94-0987 and in part by ONR-N00014-95-1-0272 e-mail:arandiga@godella.matapl.uv.es

† Departament de Matemàtica Aplicada. Universitat de València (Spain). Research supported by in part by DGICYT PB94-0987, in part by a grant from the Generalitat Valenciana and in part by ONR-N00014-95-1-0272 e-mail:donat@godella.matapl.uv.es

‡ School of Mathematical Sciences, Tel-Aviv University, Tel Aviv, Israel and Department of Mathematics, UCLA, Los Angeles CA 90024-1555 until his death August 5, 1994

1. Introduction. Fourier analysis provides a way to represent square integrable functions in terms of their sinusoidal scale-components. Fourier decomposition techniques have become basic tools for a great variety of applications in many fields of science. However, it has a drawback that renders the Fourier decomposition of an *irregular* function practically useless: It is a global decomposition; an isolated singularity dominates the behavior of all coefficients in the decomposition and prevents us from getting immediate information about the function away from the singularity.

Local-scale decompositions fare much better in this respect. Typically, one starts with a finite sequence that is somehow associated to discrete information of a given signal at the finest resolution level considered. By processing a signal at different resolution levels, one can rewrite this discrete information in a new way. The new sequence has the same cardinality as the old one (if a non-redundant scheme is used) and its coefficients represent the details at each resolution level and a final coarse approximation to the original signal.

Multiresolution representations of $L^2(R)$ functions can be computed by decomposing the signal using a wavelet orthonormal basis. In the wavelet framework, all is done by a succession of orthogonal basis transformations, therefore the inverse operation, i.e. recovering the incoming discrete signal from its multiresolution representation, is given by the adjoint matrices.

Wavelet orthonormal basis are composed of dilates and translates of a single function, the wavelet. The wavelet is intimately linked to the *scaling* function, or sometimes called the *mother* wavelet. This function satisfies a dilation relation which is in fact responsible for the properties of the multi-scale decomposition. The construction of multiresolution schemes based on orthonormal wavelet basis becomes then equivalent to a search for solutions in $L^2(R)$ of very particular dilation relations.

In [8, 9, 10] Harten develops a general framework for multiresolution representation of data. In his general framework, Harten abandons the dilation relation as the basic design tool and considers instead two operators, decimation and prediction, as the building blocks of a multiresolution scheme.

Let us consider a sequence of grids X_k corresponding (as k increases) to increasing resolution levels. The decimation operator, D_k^{k-1}, is a linear operator that yields the discrete information contents of the signal at the resolution $k-1$ from the discrete information at level k. The prediction operator, P_{k-1}^k, yields an approximation to the discrete information contents at the k-th level from the discrete information contents at level $k-1$. Thus

$$(1)\qquad \begin{aligned} &\text{(a)}\quad D_k^{k-1} \;:\; V^k \;\rightarrow\; V^{k-1}, \qquad D_k^{k-1} \text{ linear operator} \\ &\text{(b)}\quad P_{k-1}^k \;:\; V^{k-1} \;\rightarrow\; V^k, \end{aligned}$$

where V^k is a space with a denumerable basis which is related to the level of resolution specified by X_k (for example, in many one-dimensional applications $V^k = S^k$, a space of sequences of dimension related to that of the grid X_k).

The basic property that these two operators have to satisfy is

$$(2)\qquad D_k^{k-1} \cdot P_{k-1}^k = I_{k-1} \qquad \text{where } I_{k-1} \text{ is the identity operator in } V^{k-1},$$

which is nothing but a consistency relation: Predicted values at the k-th resolution level should have the same information contents as the original values, when restricted to the $k-1$st level. In addition, it is also required that D_k^{k-1} be onto. This requirement is also quite natural, it means that discrete information at each resolution level can always be thought of

as the restriction (a term which is borrowed from the multigrid terminology) of some discrete information at the next resolution level.

A sequence of decimation and prediction operators $\{D_k^{k-1}\}$ and $\{P_{k-1}^k\}$ satisfying (1) and (2) define a multiresolution transform, i.e. a (one to-one) correspondence between the original data and a multi-scale decomposition of it. The inverse multiresolution transform allows us to recover the original (discrete) data from its multiresolution representation.

The direct and inverse multiresolution transforms are described algorithmically as follows:

$v^L \quad \rightarrow \quad Mv^L \qquad$ (Encoding)

$$\text{(3)} \qquad \begin{cases} \text{Do} \quad k = L, \ldots, 1 \\ v^{k-1} = D_k^{k-1} v^k \\ d^k = G_k(v^k - P_{k-1}^k v^{k-1}) \end{cases}$$

$$Mv^L = \{v^0, d^1, \ldots, d^L\}$$

$Mv^L \quad \rightarrow \quad M^{-1}Mv^L \qquad$ (Decoding)

$$\text{(4)} \qquad \begin{cases} \text{Do} \quad k = 1, \ldots, L \\ v^k = P_{k-1}^k v^{k-1} + E_k d^k \end{cases}$$

The *scale coefficients*, d^k, are obtained from the prediction errors

$$e^k = v^k - P_{k-1}^k v^{k-1}$$

by removing the redundant information in them. Notice that

$$D_k^{k-1} e^k = D_k^{k-1}(v^k - P_{k-1}^k v^{k-1}) = 0,$$

in other words, e^k belongs to the null space of the decimation operator

$$e^k \in \mathcal{N}(D_k^{k-1}) = \{v \,|v \in V^k, \quad D_k^{k-1} v = 0\}.$$

If $\dim V^k = N_k$, then $\dim \mathcal{N}(D_k^{k-1}) = N_k - N_{k-1}$. Hence, if we select a set of basis functions in $\mathcal{N}(D_k^{k-1})$

$$\mathcal{N}(D_k^{k-1}) = \text{span}\{\mu_j^k\}_{j=1}^{N_k - N_{k-1}},$$

the prediction error e^k, which belongs to V^k and so is described in terms of N_k components, can be represented in terms of its $N_k - N_{k-1}$ coordinates in the base $\{\mu_j^k\}$:

$$e^k = \sum_{j=1}^{N_k - N_{k-1}} d_j^k \mu_j^k =: E_k d^k; \qquad d^k = G_k e^k.$$

Thus G_k computes the coordinates of the prediction error in the basis $\{\mu_j^k\}$ (which does not need to be orthogonal). Observe that $E_k G_k$ is the identity operator in $\mathcal{N}(D_k^{k-1})$.

At this point it is easy to prove that there is a one to one correspondence between v^k and $\{d^k, v^{k-1}\}$: Given v^k we evaluate

$$\text{(5)} \qquad \begin{cases} v^{k-1} &= D_k^{k-1} v^k \\ d^k &= G_k(I_k - P_{k-1}^k D_k^{k-1}) v^k. \end{cases}$$

Given v^{k-1} and d^k we recover v^k by

$$
\begin{aligned}
(6) \qquad P_{k-1}^k v^{k-1} + E_k d^k &= P_{k-1}^k D_k^{k-1} v^k + E_k G_k (I_k - P_{k-1}^k D_k^{k-1}) v^k \\
&= P_{k-1}^k D_k^{k-1} v^k + (I_k - P_{k-1}^k D_k^{k-1}) v^k \\
&= v^k.
\end{aligned}
$$

This shows that

$$v^L \overset{1:1}{\leftrightarrow} \{v^0, d^1, \ldots, d^L\} = M v^L.$$

In Harten's framework, the design of a multiresolution scheme is directly related to the choice of sequences of decimation an prediction operators, subject to (1) and (2). The construction of these sequences depends on two fundamental tools: discretization and reconstruction. The discretization operator obtains discrete information from a (non-discrete) signal at a particular resolution level. The reconstruction operator produces an approximation to that signal from the discrete values.

Let $\mathcal{F}$ be the space of functions to be subjected to a discretization process $\mathcal{D}$, which yields discrete information at the resolution level specified by the grid X. Then

$$\mathcal{D} : \mathcal{F} \longrightarrow V = \mathcal{D}(\mathcal{F}), \qquad \mathcal{R} : V \longrightarrow \mathcal{F}.$$

We require that $\mathcal{D}$ be a linear operator (it is onto by construction).

The function $\mathcal{R}\mathcal{D}f$ is regarded as an approximation to f, in the same function space to which f belongs to. A basic consistency requirement is that the reconstruction from a set of discrete data must contain exactly the same discrete information, at the specified resolution level, as the original sequence. This can be expressed as follows:

$$(7) \qquad \mathcal{D}\mathcal{R}v = v \quad \forall v \in V \qquad \equiv \qquad \mathcal{D}\mathcal{R} = I_V.$$

A sequence of discretization $\{\mathcal{D}_k\}$ can be used to define a family of decimation operators $\{D_k^{k-1}\}$. In order for this to happen, the sequence of discretization operators has to be *nested.* In plain language, the nested property implies that lower resolution levels contain no more discrete information than higher resolution levels. In mathematical terms this is expressed as:

$$(8) \qquad \mathcal{D}_k f = 0 \qquad \Rightarrow \qquad \mathcal{D}_{k-1} f = 0.$$

Each decimation operator is then defined as follows: For any $v^k \in V^k$, let $f \in \mathcal{F}$ be such that $\mathcal{D}_k f = v^k$; then $D_k^{k-1} v^k = \mathcal{D}_{k-1} f$. Since $\mathcal{D}_k$ is onto, we can express the above as

$$D_k^{k-1} \mathcal{D}_k = \mathcal{D}_{k-1}.$$

It is easy to see that this definition satisfies the properties required of a decimation operator. We would also like to stress that, in practice, the decimation step is carried out without explicit knowledge of f.

Discrete data are usually obtained from a particular discretization process. This implies that very often the *nature* of the discrete data (i.e. the way in which it was generated) dictates the appropriate multiresolution setting in which this data should be analyzed. The goal in Harten's framework is the design of multiresolution schemes that apply to all sequences, but that are particularly adequate for those obtained by the discretization process used to define the scheme.

The prediction operators are obtained from the sequences $\{\mathcal{D}_k\}$ and $\{\mathcal{R}_k\}$ as follows:

$$P_{k-1}^k v^{k-1} = \mathcal{D}_k \mathcal{R}_{k-1} v^{k-1}; \tag{9}$$

then

$$D_k^{k-1} P_{k-1}^k v^{k-1} = D_k^{k-1} \mathcal{D}_k \mathcal{R}_{k-1} v^{k-1} = \mathcal{D}_{k-1} \mathcal{R}_{k-1} v^{k-1} = v^{k-1}$$

and (2) is satisfied.

One of the main concerns in the design of a multiresolution scheme is the *quality* of the prediction. The notion of k-th scale is related to the information in v^k which cannot be predicted from v^{k-1} by *any* prediction scheme. When using a particular one, the prediction errors, and consequently the scale coefficients d^k, include a component of approximation error which is related to the *quality* or *accuracy* of the particular prediction we used.

By expressing the multiresolution scheme in terms of a sequence of discretization and reconstruction operators, the problem of finding a suitable prediction operator for a multiresolution setting can be reduced to a typical problem in approximation theory:

Knowing $\mathcal{D}_{k-1} f$, $f \in \mathcal{F}$ find a "good approximation" to $\mathcal{D}_k f$.

The relation between the prediction operator and the reconstruction procedure opens up a tremendous number of possibilities for the design of multiresolution schemes, where the primary consideration is the selection of the appropriate discretization. We can consider not only linear reconstruction procedures, as in most wavelet-type multiresolution algorithms, but also non-linear (data dependent) ones.

Linear multiresolution schemes within Harten's framework have been widely studied in [9, 10, 11] and [3]. In this series of works it is shown that biorthogonal wavelets can be thought of as the "uniform constant coefficient" case of the general framework. It corresponds to a choice of some weighted-average discretization in R together with a particular reconstruction procedure, which is in fact the natural one form the functional analysis point of view ($\mathcal{R}_k \mathcal{D}_k$ is a projection). Orthogonal wavelets are also obtained from Harten's framework by imposing an additional constraint: the discretization and reconstruction operators are based on the *same* weight-function.

Unlike the classical wavelet theory, which applies to the infinite domain R, Harten's formulation is suitable for both the finite and the infinite case. Furthermore, wavelets use translates and dilates of a single function leads to a natural restriction to uniform grids. Harten's nested discretization framework removes the need to discretize on the dyadic sequence of uniform grids in R and allows for discretizations in unstructured meshes in R^m (see [2]).

Relations (5) and (6) are the basic encoding and decoding steps of a multiresolution scheme. In electrical engineering terms, (5) and (6) are the analysis and synthesis steps of a sub-band filtering scheme with exact reconstruction. The operator D_k^{k-1}plays the role of a low-pass filter and the operator $G_k(I_k - P_{k-1}^k D_k^{k-1})$ that of a band-pass filter. Usually, these filters are linear and of convolution type (this is exactly the situation within the wavelet framework).

The whole purpose of sub-band filtering is of course not to just decompose and reconstruct. The goal of the game is to do some compression or processing between the decomposition and reconstruction stages. In this respect, Harten's framework is far more flexible than the wavelet framework. The reconstruction operator (and thus the prediction) is not required to be linear, thus it is possible to obtain adaptive (data-dependent) multiresolution representations which fit the approximation to the local nature of the data. On the

other hand, the only adaptativity which is possible within the theory of wavelets is through redundant "dictionaries".

There is now a variety of data-dependent approximation techniques (e.g. the ENO interpolatory technique of [9]) which are designed to minimize regions of low accuracy in the reconstruction in the presence of isolated singularities. When dealing with 'irregular' signals, adaptive reconstruction techniques can reduce the approximation error component in d_j^k, thus leading to better compression rates than their linear counterparts.

In this paper we describe and analyze a class of non-linear multiresolution schemes for the hat-average multiresolution setting. These schemes are based on the Essentially-Non-Oscillatory (ENO) interpolatory procedure described in [9].

The paper is organized as follows: The class of non-linear reconstruction techniques we use as design tools is described in Section 2. We briefly review the ENO interpolatory procedure and Harten's Subcell-Resolution technique.

In Section 3 we review some basic results, obtained in [3], about the hat-average multiresolution setting and set the notation for the remainder of the paper. The ENO-Reconstruction with Subcell Resolution technique for the hat-average multiresolution framework is described in Section 4. Special attention is paid, in Section 5, to the application of the Subcell Resolution technique to *weak* singularities.

The stability theory developed in [12] does not apply to non-linear prediction operators. The question of stability for the non-linear multiresolution schemes we design is considered in Section 6.

In Section 7 we show various numerical experiments with comparisons, and finally some conclusions are drawn in Section 8.

2. Nonlinear Reconstruction Techniques. The scale coefficients are directly related to the prediction errors, which measure our success in using the reconstruction procedure to climb up the ladder from low-resolution to high-resolution levels.

If $p \in \mathcal{F}$ is a function for which $\mathcal{R}_{k-1}$ is exact, i.e.

$$\mathcal{R}_{k-1}(\mathcal{D}_{k-1}p) = p$$

we have likewise

$$P_{k-1}^k(\mathcal{D}_{k-1}p) = \mathcal{D}_k\mathcal{R}_{k-1}\mathcal{D}_{k-1}p = \mathcal{D}_k p,$$

i.e., the prediction P_{k-1}^k is also exact on the discrete values associated to the function p. The quality, or accuracy, of the prediction can thus be judged by the class of functions in $\mathcal{F}$ for which the reconstruction from their discrete values is exact.

If the set of exactness for the reconstruction operators includes all polynomials of degree $p-1$, typically one has also

$$\mathcal{R}_k \bar{f}^k(x) = f(x) + O(h_k^p) \tag{10}$$

in regions where $f(x)$ is smooth. We say then that the reconstruction operator is of *order* p. The accuracy of the reconstruction technique plays a key role in the efficiency of data compression algorithms of the type (50) and (51).

An isolated singularity affects the accuracy of the reconstruction in a region whose extent depends heavily on the type of the reconstruction procedure. For example, the effect of a discontinuity is felt everywhere (to a greater or lesser degree) when using a truncated Fourier series.

In [8, 9, 10] and [3] many of the reconstruction procedures considered are based on piecewise polynomial interpolation techniques. For these, the extent of the low accuracy region around a singularity depends on the stencil of points used to construct the polynomial pieces. It is clear that whenever the stencil crosses the singularity, (10) fails to hold.

Data-independent (linear) interpolatory techniques use a fixed stencil to construct each polynomial piece. Since the number of points in the stencil increases with polynomial degree (order of the interpolation), so does the extent of the low accuracy region.

In [12], Harten et al. introduce a data-dependent piecewise-polynomial interpolation technique which they refer to as Essentially Non-Oscillatory (ENO) interpolation. The basic idea of the ENO technique is to enlarge the region of high accuracy by constructing the piecewise polynomial interpolants using only information from regions of smoothness of the interpolated function.

For piecewise smooth signals with a finite number of singularities, adaptive, data dependent reconstructions of order p manage to keep relation (10) valid over a larger region than linear (= data independent) reconstructions of the same order. This implies that the approximation error component in the scale coefficients is smaller, thus leading to schemes with better compression properties.

Data compression algorithms based on cell-averaged multiresolution and ENO reconstructions applied to discontinuous piecewise smooth signals, give much better compression rates than the corresponding algorithms with linear reconstructions (see [8, 11, 6]). Moreover, Harten shows in [8, 11] that the cell-average discretization enables us to get a good approximation even in cells which contain a jump discontinuity by using the Subcell-Resolution (SR) technique of [7].

In the same fashion, we shall see that ENO reconstruction (also combined with SR) techniques in the hat-averaged multiresolution context lead to very efficient data compression algorithms for piecewise smooth signals with a finite number of δ-singularities. The space of such functions is used in vortex methods for the numerical solution of fluid dynamics problems.

For the sake of completeness, in the remainder of this section we describe briefly the ENO interpolation technique and Harten's Subcell Resolution.

2.1. ENO Interpolation. To make the presentation simpler, we consider a grid $X = \{x_i\}$ in $[0,1]$ with uniform spacing $h = x_{i+1} - x_i$ (see [1, 13] for generalizations to non-uniform grids an also to higher dimensions).

Let $H(x) \in C[0,1]$. Using the notation of section 3, we call $\tilde{\mathcal{D}}H = (H_j)_j$, where $H_j = H(x_j)$. Let $I(x; \tilde{\mathcal{D}}H)$ be any piecewise polynomial function that interpolates $H(x)$ on the grid X.

If the interpolatory technique is of order r, we have

$$I(x; \tilde{\mathcal{D}}H) = q_j(x; \tilde{\mathcal{D}}H) \qquad \text{for} \quad x \in [x_{j-1}, x_j],$$

where $q_j(x; \tilde{\mathcal{D}}H)$ is a polynomial of degree $r-1$ such that $q_j(x_{j-1}; \tilde{\mathcal{D}}H) = H_{j-1}$ and $q_j(x_j; \tilde{\mathcal{D}}H) = H_j$. The set of r grid points used to construct the polynomial piece $q_j(x; \tilde{\mathcal{D}}H)$ forms the *stencil* , $\mathcal{S}_j$, associated to the interval $[x_{j-1}, x_j]$. The grid points x_{j-1} and x_j must always belong to $\mathcal{S}_j$.

The essential feature of the ENO interpolatory technique is a stencil selection procedure that attempts to choose the stencil $\mathcal{S}_j$ within a region of smoothness of $H(x)$.

For each interval $[x_{j-1}, x_j]$, we consider all possible stencils of $r \geq 2$ points that include x_{j-1} and x_j,

$$\{x_{j-r+1}, \ldots, x_j\}, \cdots, \{x_{j-1}, \ldots, x_{j+r-2}\}$$

and assign to it the stencil for which $H(x)$ is "smoother" in some sense. We will do this by fixing $i(j)$, an index that marks the initial point of the stencil. For notational purposes, we assume that $i(j)$ is the second point in the final stencil. Notice that if $r = 2$, $\mathcal{S}_j = \{x_{j-1}, x_j\}$ and no selection technique is needed. We assume then that $r > 2$.

In [9], the authors describe two stencil selection procedures,

Algorithm I. Hierarchical choice of stencil.

$$\begin{cases} i_0(j) = j \\ \\ i_1(j) = \begin{cases} i_0(j) - 1 & \text{if} \quad |H(x_{j-2}, x_{j-1}, x_j)| < |H(x_{j-1}, x_j, x_{j+1})| \\ i_0(j) & \text{otherwise} \end{cases} \\ \\ \begin{cases} DO \quad l = 1, r-3 \\ \\ i_{l+1}(j) = \begin{cases} i_l(j) - 1 & \text{if} \quad |H(x_{i_l(j)-2}, \ldots, x_{i_l(j)+l})| < |H(x_{i_l(j)-1}, \ldots, x_{i_l(j)+l+1})| \\ i_l(j) & \text{otherwise} \end{cases} \end{cases} \\ \\ i(j) = i_{r-2}(j). \end{cases}$$

Algorithm II. Non hierarchical choice of the stencil.

$$\begin{cases} \text{Choose } i(j) \text{ so that} \\ |H(x_{i(j)-1}, \ldots, x_{i(j)+r-2})| = \min\{|H(x_{l-1}, \ldots, x_{l+r-2})|, j - r + 2 \le l \le j\}. \end{cases}$$

Notice that if $j - r + 2 \le i(j) \le j$, then x_{j-1}, $x_j \in \mathcal{S}_j$.

The hierarchical choice of the stencil is the preferred one in most situations. Algorithm II chooses the stencil according to the monotonicity properties of $H^{(k)}$, and its performance in the pre-asymptotic range is, in general, poorer than that of Algorithm I. In our context, this becomes very important since we shall be using the ENO technique on various resolution levels, some of which may well be in the pre-asymptotic range.

Let us assume that $H(x)$ is a picewise continuous function and that $H'(x)$ has discontinuity at $x_d \in [x_{j-1}, x_j]$ (we say then that $H(x)$ has a *corner* at x_d). When $[H']_{x_d} = H'(x_d + 0) - H'(x_d - 0) = O(1)$, an analysis of the stencil selection procedure (see e.g. [5]) reveals that both Algorithm I and II lead to stencils such that

$$\mathcal{S}_{j-1} \cap \mathcal{S}_{j+1} = \emptyset.$$

This confirms that both stencil selection procedures lead to interpolatory polynomials that satisfy

$$H(x) = q_l(x; \tilde{\mathcal{D}}H) + O(h^r ||H^r||) \qquad x \in [x_{l-1}, x_l], \quad l \le j-1, \quad l \ge j+1.$$

However, the smooth polynomial $q_j(x; \tilde{\mathcal{D}}H)$ can only be a first order approximation to the function $H(x)$ at the $[x_{j-1}, x_j]$ cell.

On the other hand, interpolatory techniques based on a fixed choice of stencil lead to polynomial interpolants q_l that are only first order approximations to $H(x)$ as soon as their stencil crosses x_d. The accuracy of the piecewise polyomial interpolant is thus degraded over a large region around the singularity (its range depends on the degree of the polynomial pieces, i.e. the number of points in $\mathcal{S}_j$).

It is proven in [5] that, if the only singularities of $H(x)$ are corners and they are well separated (it is possible to choose a stencil in the smooth part of the function), then the ENO interpolation procedure leads to a piecewise interpolant that satisfies

$$\frac{d^m}{dx^m} I(x \pm 0; \tilde{\mathcal{D}} H) = \frac{d^m}{dx^m} H(x) + O(h^{r-m}) \qquad 0 \le m \le r-1 \tag{11}$$

except when x belongs to an interval containing a corner. As a result, the accuracy of the ENO piecewise polynomial interpolant is mantained over the largest possible region.

If we know the location of the singularity within the cell (or a sufficiently good approximation to it), the definition of the piecewise interpolant $I(x; \tilde{\mathcal{D}} H)$ can be modified to keep the relation

$$H(x) = I(x; \tilde{\mathcal{D}} H) + O(h^r)$$

valid over an even larger region. This is the basic idea behind Harten's Subcell Resolution technique.

2.2. The Subcell Resolution Technique. Let us assume that $H(x)$ is a continuous function with a corner at $x_d \in (x_{j-1}, x_j)$. Then, the ENO interpolants $q_{j\pm1}(x; \tilde{\mathcal{D}} H)$ satisfy

$$H(x) = q_{j-1}(x; \tilde{\mathcal{D}} H) + O(h^r) \qquad x \in [x_{j-2}, x_{j-1}] \tag{12}$$

$$H(x) = q_{j+1}(x; \tilde{\mathcal{D}} H) + O(h^r) \qquad x \in [x_j, x_{j+1}]. \tag{13}$$

The location of the corner, x_d, can be recovered using the following function:

$$G_j(x) := q_{j+1}(x; \tilde{\mathcal{D}} H) - q_{j-1}(x; \tilde{\mathcal{D}} H). \tag{14}$$

Using Taylor expansions in regions of smoothness, it is not hard to prove that

$$G_j(x_{j-1}) \cdot G_j(x_j) = a \cdot (a-1)[H']^2_{x_d} h^2 + O(h^3)$$

where $x_d = x_j - ah$.

Therefore, if h is sufficiently small, there is a root of G_j in (x_{j-1}, x_j); let $\theta_j \in (x_{j-1}, x_j)$ be such that $G_j(\theta_j) = 0$. We consider θ_j to be an approximation to x_d, but how good is this approximation? Let us consider the special case

$$H(x) = \begin{cases} P_L(x) & x \le x_d \\ P_R(x) & x \ge x_d \end{cases} \tag{15}$$

$$P_L(x_d) = P_R(x_d), \qquad P_L'(x_d) \neq P_R'(x_d)$$
$$\max(\deg(P_L), \deg(P_R)) \le r-1.$$

By construction, we must have then

$$q_{j-1}(x; \tilde{\mathcal{D}} H) = P_L(x), \qquad q_{j+1}(x; \tilde{\mathcal{D}} H) = P_R(x).$$

which implies that $\theta_j = x_d$. In the general case, it can be proven (see [7] or [5]) that

$$|\theta_j - x_d| = O(h^r).$$

Thus, using the ENO polynomial pieces at each side of the singularity, we can recover the location of an isolated discontinuity in the derivative of a continuous function, up to the

order of the truncation error. This information can be used to modify the polynomial piece corresponding to the cell $[x_{j-1}, x_j]$ as follows: Instead of taking the polynomial $q_j(x; \tilde{\mathcal{D}}H)$ as the approximation of $H(x)$ at this interval, we extend the polynomial pieces at the left and right neighboring intervals up to the point θ_j, where they intersect. The new piecewise polynomial interpolant has the following form

$$I^{SR}(x; \tilde{\mathcal{D}}H) = \begin{cases} q_l(x; \tilde{\mathcal{D}}H) & x \in [x_{l-1}, x_l], \quad l \neq j \\ q_{j-1}(x; \tilde{\mathcal{D}}H) & x \in [x_{j-1}, \theta_j] \\ q_{j+1}(x; \tilde{\mathcal{D}}H) & x \in [\theta_j, x_j]. \end{cases} \tag{16}$$

It is then clear that

$$I^{SR}(x_l; \tilde{\mathcal{D}}H) = H(x_l), \qquad x_l \in X$$

$$\frac{d^m}{dx^m} I^{SR}(x \pm 0; \tilde{\mathcal{D}}H) = \frac{d^m}{dx^m} H(x) + O(h^{r-m}), \qquad 0 \leq m \leq r-1$$

at all points except for an $O(h^r)$ band around x_d which is now the only region in which the accuracy is degraded (instead of the whole interval $[x_{j-1}, x_j]$). It follows that if $H(x)$ is as in (15) then $I^{SR}(x; \tilde{\mathcal{D}}H) = H(x)$, i.e. the modified reconstruction is exact.

The basic principle underlying the SR technique is in fact very simple:

Use accurate reconstructions at the cells neighboring a singularity to recover the singularity within the cell

and it can be applied also to weaker singularities. Suppose that $H(x)$ has a discontinuity in its $q+1$st derivative ($q < r$), i.e. $H(x) \in C^q$ and $[H^{(q+1)}]_{x_d} = O(1)$ where $x_d \in [x_{j-1}, x_j]$. If the polynomial functions $q_{j-1}(x; \tilde{\mathcal{D}}H)$ and $q_{j+1}(x; \tilde{\mathcal{D}}H)$ are constructed using only data from the smooth part of $H(x)$, or in other words if $\mathcal{S}_{j-1} \cap \mathcal{S}_{j+1} = \emptyset$, then we have

$$\frac{d^m}{dx^m} q_{j-1}(x; \tilde{\mathcal{D}}H) = \frac{d^m}{dx^m} H(x) + O(h^{r-m}) \qquad x \in [x_{j-2}, x_{j-1}] \qquad 0 \leq m \leq r-1$$

$$\frac{d^m}{dx^m} q_{j+1}(x; \tilde{\mathcal{D}}H) = \frac{d^m}{dx^m} H(x) + O(h^{r-m}) \qquad x \in [x_j, x_{j+1}] \qquad 0 \leq m \leq r-1$$

Using again Taylor expansions, we can prove that

$$G_j^{(q)}(x_j) \cdot G_j^{(q)}(x_{j-1}) < 0.$$

Thus, there is a root of $G^{(q)}(x)$ in $[x_{j-1}, x_j]$. Furthermore, if the root is θ_j, it is not hard to prove (see [5]) that

$$|\theta_j - x_d| = O(h^{r-q}).$$

It follows that replacing $I(x; \tilde{\mathcal{D}}H)$ by $I^{SR}(x; \tilde{\mathcal{D}}H)$ in (16) with θ_j being now the root of $G^{(q)}(x)$ in $[x_{j-1}, x_j]$, leads to a reconstruction technique which is exact for the corresponding piecewise polynomial problem (15) with

$$P_L^{(m)}(x_d) = P_R^{(m)}(x_d), \quad 0 \leq m \leq q \qquad \text{and} \qquad P_L^{(q+1)}(x_d) \neq P_R^{(q+1)}(x_d).$$

The key to the success of the SR technique is the accuracy of the polynomial pieces $q_{j\pm1}$. The ENO technique ensures (12) and (13) when the singularity is a corner. However, when

dealing with weaker singularities, Algorithm I might lead to a selection of stencil such that $\mathcal{S}_{j-1}$ or $\mathcal{S}_{j+1}$ (or both) cross the singularity. The phenomenon is analyzed in detail in [5] where it is observed that, to maintain the accuracy of the polynomial pieces, one needs to switch to Algorithm II in cells neighboring weak singularities.

In practice, we like to work with Algorithm I because of its better overall behavior in regions of smoothness. Thus one needs to identify those cells that are suspected of harboring a weak discontinuity and recompute the polynomial pieces at the neighboring cells.

We would like to finish this section with a remark: If $H(x)$ has a corner at a grid point, say x_j, then q_j and q_{j+1} are accurate representations of $H(x)$ within their respective intervals; however if x_j is a weaker discontinuity, the results of [5] indicate that $\mathcal{S}_j$ and/or $\mathcal{S}_{j+1}$ might cross the singularity. This leads to a degradation of the accuracy of q_j and/or q_{j+1}. We address this issue in section 5.

3. Basic Background on the Hat-average Multiresolution Framework. This section is a brief review of section 6 in Part I [3]. Here we only describe those elements of the hat-average setting that we find necessary for the development of this paper. We refer the reader to [3] for more details and for proofs of all the facts we state below.

Let us consider the unit interval $[0,1]$ and the sequence of nested dyadic grids $X^k = \{x_i^k\}_{i=0}^{J_k}$, $x_i^k = ih_k$, $h_k = 2^{-k}h_0$, $J_k = 2^k J_0$.

The discretization procedure is based on integrating against scaled translates of the hat function:

$$\omega(x) = \begin{cases} 1+x & -1 \le x \le 0 \\ 1-x & 0 \le x \le 1 \\ 0 & \text{otherwise} \end{cases} \tag{17}$$

that is:

$$(\mathcal{D}_k f)_i = \bar{f}_i^k = < f, \omega_i^k >, \qquad \omega_i^k = \frac{1}{h_k}\omega(\frac{x}{h_k} - i). \tag{18}$$

Notice that it is sufficient to consider weighted averages $\bar{f}_i^k$ for $1 \le i \le N_k = J_k - 1$ since these averages contain information on f over the whole interval $[0,1]$. Moreover, since the hat function is continuous, a finite number of (isolated) δ-type singularities are allowed. Thus

$$\mathcal{D}_k : \mathcal{F} \longrightarrow S^k,$$

where $\mathcal{F}$ is the space of piecewise smooth functions in $[0,1]$ with a finite number of δ-type singularities in $(0,1)$, and S^k is the space of finite sequences of $N_k = J_k - 1$ components.

The hat function satisfies the following dilation relation:

$$\omega(x) = \frac{1}{2}[\omega(2x-1) + 2\omega(2x) + \omega(2x+1)]. \tag{19}$$

This implies that

$$\bar{f}_i^{k-1} = \frac{1}{4}\bar{f}_{2i-1}^k + \frac{1}{2}\bar{f}_{2i}^k + \frac{1}{4}\bar{f}_{2i+1}^k. \tag{20}$$

Therefore the decimation matrix (an $N_{k-1} \times N_k$ matrix) is given explicitly by the following expression:

$$(D_k^{k-1})_{ij} = \frac{1}{4}\delta_{2i-1,j} + \frac{1}{2}\delta_{2i,j} + \frac{1}{4}\delta_{2i+1,j}. \tag{21}$$

Because of the dilation relation satisfied by the hat function, the prediction errors satisfy

$$e^k_{2i} = -\frac{1}{2}e^k_{2i-1} - \frac{1}{2}e^k_{2i+1}. \tag{22}$$

This leads to the following algorithmic description of the transfer operators G_k and E_k:

$$d^k = G_k e^k \qquad d^k_j = e^k_{2j-1}, \quad 1 \le j \le J_{k-1} \tag{23}$$

$$e^k = E_k d^k \qquad \begin{cases} e^k_{2j-1} &= d^k_j & 1 \le j \le J_{k-1} \\ e^k_{2j} &= -\frac{1}{2}(d^k_j + d^k_{j+1}) & 1 \le j \le J_{k-1} - 1. \end{cases} \tag{24}$$

To complete the construction of a multiresolution scheme, we need a working definition of the prediction operators. This is accomplished by the *reconstruction via second primitive technique*. A brief description of the technique is as follows:

Let f be a piecewise smooth function in $[0,1]$ with a finite number of δ-jumps in $(0,1)$. Define its "second primitive" as

$$H(x) = \int_0^x \int_0^y f(z)dzdy. \tag{25}$$

Then $H(x)$ is a continuous piecewise smooth function which satisfies the following relation:

$$\bar{f}^k_i =< f, \omega^k_i >= \frac{1}{h^2_k}(H^k_{i+1} - 2H^k_i + H^k_{i-1}), \quad 1 \le i \le J_k - 1, \tag{26}$$

$$\text{where} \quad H^k_l = H(x^k_l) \quad 0 \le l \le J_k$$

The lower integration limits are irrelevant to the final outcome of the algorithm. Given the values $H^k_0 = H(0)$ and $H^k_{J_k} = H(1)$, relation (26) establishes a one-to-one correspondence between the sets $\{\bar{f}^k_i\}_{i=1}^{J_k-1}$ and $\{H^k_i\}_{i=1}^{J_k-1}$. In fact,

$$h^2_k \bar{f}^k = MH^k, \qquad M_{i,j} = \begin{cases} -2 & i = j \\ 1 & |i-j| = 1 \\ 0 & \text{else.} \end{cases} \tag{27}$$

Thus, knowledge of the hat-averages of a given function $f \in \mathcal{F}$ is equivalent to knowledge of the point values of its second primitive (25). We can then interpolate the point-values of the "second primitive" by any interpolation procedure $I_k(x; H^k)$ and define

$$(\mathcal{R}_k \bar{f}^k)(x) = \frac{d^2}{dx^2} I_k(x; H^k). \tag{28}$$

In general, $I_k(x; H^k)$ is a continuous, piecewise smooth function. Its first derivative will also be a piecewise smooth function possibly with discontinuities at the grid points of the k-th level. Thus its second derivative must be considered in the distribution sense.

If the interpolatory function is defined as

$$I_k(x; H^k) = I_{k,j}(x; H^k) \qquad \text{for } x \in [x^k_{j-1}, x^k_j] \tag{29}$$

we have (in the distribution sense)

$$(\mathcal{R}_k \bar{f}^k)(x) = \tilde{I}_k(x) + \sum_{j=1}^{J_k-1} s^k_j \delta(x - x^k_j) \tag{30}$$

where $\tilde{I}_k$ is defined as

$$\tilde{I}_k(x) = \frac{d^2}{dx^2} I_{k,j}(x; H^k) \qquad \text{for } x \in [x_{j-1}^k, x_j^k], \tag{31}$$

and

$$s_j^k = \left[\frac{d}{dx} I_{k,j+1}(x; H^k) - \frac{d}{dx} I_{k,j}(x; H^k)\right]_{x=x_j^k} = I_k{}'(x_j^k + 0; H^k) - I_k{}'(x_j^k - 0; H^k). \tag{32}$$

We proved in Part I [3] that $\mathcal{R}_k$ in (30) is a proper reconstruction procedure in the hat-weighted multiresolution setting, that is, it satisfies $\mathcal{D}_k \mathcal{R}_k = I_k$. Moreover, if the order of the interpolation is r, then the order of $\mathcal{R}_k$ in (28) is $p = r - 2$. The prediction operator is now computed from $\mathcal{R}_k$ using (9),

$$\begin{aligned} (P_{k-1}^k \bar{f}^{k-1})_j &= (\mathcal{D}_k \mathcal{R}_{k-1} \bar{f}^{k-1})_j = < \mathcal{R}_{k-1} \bar{f}^{k-1}, \omega_j^k > = \\ &= < \tilde{I}_{k-1}, \omega_j^k > + \sum_{l=1}^{J_{k-1}-1} s_l^{k-1} < \delta(x - x_l^{k-1}), \omega_j^k >, \quad 1 \le j \le J_k - 1. \end{aligned}$$

which leads to (for $1 \le j \le J_k - 1$)

$$(P_{k-1}^k \bar{f}^{k-1})_j = \frac{1}{h_k^2} \left(I_{k-1}(x_{j-1}^k; H^{k-1}) - 2 I_{k-1}(x_j^k; H^{k-1}) + I_{k-1}(x_{j+1}^k; H^{k-1}) \right). \tag{33}$$

Once all the necessary ingredients of the multiresolution scheme have been specified, we can give an explicit description of the hat-based multiresolution transform and its inverse,

$\bar{f}^L \quad \rightarrow \quad M \bar{f}^L$ (Encoding)

$$\left\{ \begin{array}{ll} \text{Do} \quad k = L, 1 & \\ \quad \bar{f}_i^{k-1} = \frac{1}{4}(\bar{f}_{2i-1}^k + 2\bar{f}_{2i}^k + \bar{f}_{2i+1}^k), & 1 \le i \le J_{k-1} - 1 \\ \quad d_i^k = \bar{f}_{2i-1}^k - (P_{k-1}^k \bar{f}^{k-1})_{2i-1}, & 1 \le i \le J_{k-1} \end{array} \right. \tag{34}$$

$M \bar{f}^L \quad \rightarrow \quad M^{-1} M \bar{f}^L$ (Decoding)

$$\left\{ \begin{array}{ll} \text{Do} \quad k = 1, L & \\ \quad \bar{f}_{2i-1}^k = (P_{k-1}^k \bar{f}^{k-1})_{2i-1} + d_i^k, & 1 \le i \le J_{k-1} \\ \quad \bar{f}_{2i}^k = 2\bar{f}_i^{k-1} - \frac{1}{2}(\bar{f}_{2i-1}^k + \bar{f}_{2i+1}^k), & 1 \le i \le J_{k-1} - 1 \end{array} \right. \tag{35}$$

To derive these algorithms we have used the fact that

$$\bar{f}_{2i}^k = (P_{k-1}^k \bar{f}^{k-1})_{2i} + (E_k d^k)_{2i} = 2\bar{f}_i^{k-1} - \frac{1}{2}(\bar{f}_{2i-1}^k + \bar{f}_{2i+1}^k).$$

The description of the prediction operator in terms of the reconstruction via "second primitive" links the hat-average and the interpolatory multiresolution settings considered in [8, 9, 10]. The interpolation technique used to define $\mathcal{R}_k$ in (28) provides also a reconstruction operator for an interpolatory setting. Thus, the application of a hat-average multiresolution scheme to a function $f \in \mathcal{F}$ is intimately connected to the application of a specific interpolatory multiresolution scheme to its second primitive. Both settings play a role in our later development, thus to distinguish between the two of them we reserve the symbols $\mathcal{D}_k$, $\mathcal{R}_k$,

D_k^{k-1} and P_{k-1}^k for the hat-average multiresolution setting and the symbols $\tilde{\mathcal{D}}_k$, $\tilde{\mathcal{R}}_k$, $\tilde{D}_k^{k-1}$, $\tilde{P}_{k-1}^k$ for the interpolatory setting, i.e. given a function $H(x) \in \mathcal{C}[0,1]$, we have

$$
\begin{aligned}
(\tilde{\mathcal{D}}_k H)_i &= H_i^k = H(x_i^k), && 0 \le i \le J_k \\
\tilde{\mathcal{R}}_k H^k(x) &= I_k(x; H^k) \equiv I_k(x; \tilde{\mathcal{D}}_k H), && x \in [0,1] \\
(\tilde{D}_k^{k-1} H^k)_i &= H_{2i}^k = H_i^{k-1}, && 0 \le i \le J_{k-1} \\
(\tilde{P}_{k-1}^k H^{k-1})_i &= I_{k-1}(x_i^k; H^{k-1}), && 0 \le i \le J_k
\end{aligned} \tag{36}
$$

4. ENO Reconstruction with Subcell Resolution in the Hat-average Context. The *reconstruction via second primitive* technique can be carried out using *any* interpolatory procedure. We observed in Section 2 that adaptive non-linear interpolatory techniques such as the ENO interpolation maintain the full accuracy of the approximation over a much larger region than linear techniques of the same order. Thus ENO-based reconstruction operators have better compression capabilities than their linear counterparts.

The region where the piecewise polynomial interpolant attains its full accuracy can be maximized using Harten's SR technique. In this section, we show that using the ENO interpolation with Subcell Resolution as the basic interpolatory procedure in (28) leads to a proper reconstruction procedure within the hat-average framework (i.e. (7) is satisfied).

We intend to use the ENO-SR reconstruction as our approximation tool in the Hat-average multiresolution setting. In order to do this, we proceed to describe the prediction operator related to this reconstruction procedure.

To fix ideas, we consider a grid $X = \{x_i\}$ in $[0,1]$ with uniform spacing $h = x_{i+1} - x_i$ and assume that

$$f(x) = P(x) + \alpha\delta(x - x_d)$$

where $P(x)$ is smooth and $x_d \in (x_{j-1}, x_j)$. Its second primitive (25) has the following form

$$H(x) = Q(x) + \alpha(x - x_d)_+$$

where $Q(x)$ is a smooth function such that $Q'' = P$ and

$$(x-z)_+ = \begin{cases} x - z & \text{if} \quad x > z \\ 0 & \text{otherwise.} \end{cases}$$

Hence, $H(x)$ has a corner at x_d ($[H']_{x_d} = \alpha$) and is smooth otherwise. An ENO interpolation of $H(x)$ of order r leads to a piecewise polynomial function $I(x; \tilde{\mathcal{D}}H)$ satisfying (11) except at the interval containing x_d. Notice that

$$s_l = [I'(x; \tilde{\mathcal{D}}H)]_{x_l} = I'(x_l + 0; \tilde{\mathcal{D}}H) - I'(x_l - 0; \tilde{\mathcal{D}}H) = O(h^{r-1}) \qquad l \neq j-1, j.$$

REMARK 4.1. *Because of (26), second and higher order divided diferences of $H(x)$ on the grid X can be expressed in terms of $(\mathcal{D}f)$ and its divided diferences. Hence, the ENO stencil selection procedure can be carried out without explicit knowledge of $(\tilde{\mathcal{D}}H) = (H(x_j))$.*

The SR technique substitutes the ENO piecewise polynomial interpolant, $I(x; \tilde{\mathcal{D}}H)$, by $I^{SR}(x; \tilde{\mathcal{D}}H)$ as defined in (16). Using Lemma 6.1 in [3] and our observations in section 2, we can easily derive the ENO-SR reconstruction operator in the hat-average context:

$$\mathcal{R}^{SR}(x; \mathcal{D}f) = \frac{d^2}{dx^2} I^{SR}(x; \tilde{\mathcal{D}}H) = \tilde{I}^{SR}(x; \tilde{\mathcal{D}}H) + \sum_{i \neq j-1, j} s_i \delta(x - x_i) + \hat{s}_j \delta(x - \theta_j) \tag{37}$$

where

$$\theta_j \in (x_{j-1}, x_j), \qquad G_j(\theta_j) = 0, \qquad G_j(x) = q_{j+1}(x; \tilde{\mathcal{D}}H) - q_{j-1}(x; \tilde{\mathcal{D}}H), \tag{38}$$

$$\tilde{I}^{SR}(x; \tilde{\mathcal{D}}H) = \begin{cases} \frac{d^2}{dx^2} q_l(x; \tilde{\mathcal{D}}H) & x \in [x_{l-1}, x_l]; \quad l \neq j \\ \frac{d^2}{dx^2} q_{j-1}(x; \tilde{\mathcal{D}}H) & x \in [x_{j-1}, \theta_j] \\ \frac{d^2}{dx^2} q_{j+1}(x; \tilde{\mathcal{D}}H) & x \in [\theta_j, x_j] \end{cases} \tag{39}$$

and

$$\begin{aligned} s_l &= \left[\frac{d}{dx} q_{l+1}(x; \tilde{\mathcal{D}}H) - \frac{d}{dx} q_l(x; \tilde{\mathcal{D}}H)\right]_{x=x_l} \qquad l \neq j-1, j \\ \hat{s}_j &= \left[\frac{d}{dx} q_{j+1}(x; \tilde{\mathcal{D}}H) - \frac{d}{dx} q_{j-1}(x; \tilde{\mathcal{D}}H)\right]_{x=\theta_j}. \end{aligned}$$

The SR technique is local: $\mathcal{R}^{SR}(x; \mathcal{D}f)$ coincides with $\mathcal{R}(x; \mathcal{D}f)$ (the reconstruction obtained by differentiating the ENO interpolant $I(x; \tilde{\mathcal{D}}H)$) except at the cell containing the singularity. Our analysis in section 2.2 shows that $\mathcal{R}^{SR}(x; \mathcal{D}f)$ is exact when $P(x)$ is a polynomial function such that $\deg(P) \leq p - 1 = r - 3$.

Let us prove that $\mathcal{R}^{SR}(x; \mathcal{D}f)$ satisfies $\mathcal{D}\mathcal{R}^{SR} = I$. Observe that

$$< \mathcal{R}^{SR}(x; \mathcal{D}f), \omega_l > = < \tilde{I}^{SR}(x; \tilde{\mathcal{D}}H), \omega_l > + \sum_{i \neq j, j-1} s_i < \delta(x - x_i), \omega_l > + \hat{s}_j < \delta(x - \theta_j), \omega_l > .$$

The local character of the SR technique implies then

$$(\mathcal{D}\mathcal{R}^{SR}(x; \mathcal{D}f))_l = < \mathcal{R}^{SR}(x; \mathcal{D}f)), \omega_l > = < \mathcal{R}(x; \mathcal{D}f)), \omega_l > = (\mathcal{D}f)_l \quad l \neq j-1, j. \tag{40}$$

On the other hand, integration by parts shows that

$$\begin{aligned} (\mathcal{D}\mathcal{R}^{SR}(x; \mathcal{D}f))_j &= < \tilde{I}^{SR}(x; \tilde{\mathcal{D}}H), \omega_j > + \hat{s}_j < \delta(x - \theta_j), \omega_j > \\ &= -\hat{s}_j \omega_j(\theta_j)) + \frac{1}{h^2}[H(x_{j+1}) - 2H(x_j) + H(x_{j-1})] \\ &\quad + \frac{1}{h^2}[q_{j+1}(\theta_j, \tilde{\mathcal{D}}H) - q_{j-1}(\theta_j; \tilde{\mathcal{D}}H)] + \hat{s}_j \omega_j(\theta_j) \end{aligned}$$

i.e.

$$(\mathcal{D}\mathcal{R}^{SR}(x; \mathcal{D}f))_j = (\mathcal{D}f)_j + \frac{1}{h^2} G_j(\theta_j) = (\mathcal{D}f)_j. \tag{41}$$

In the same fashion, it is easy to see that

$$(\mathcal{D}\mathcal{R}^{SR}(x; \mathcal{D}f))_{j-1} = (\mathcal{D}f)_{j-1} - \frac{1}{h^2} G_j(\theta_j) = (\mathcal{D}f)_{j-1}. \tag{42}$$

Relations (40), (41) and (42) prove our claim.

To use the ENO-SR reconstruction technique as our approximation tool in the hat-average multiresolution setting, we need a working description of the prediction operator which is defined as $\hat{P}_{k-1}^k := \mathcal{D}_k \mathcal{R}_{k-1}^{SR}$.

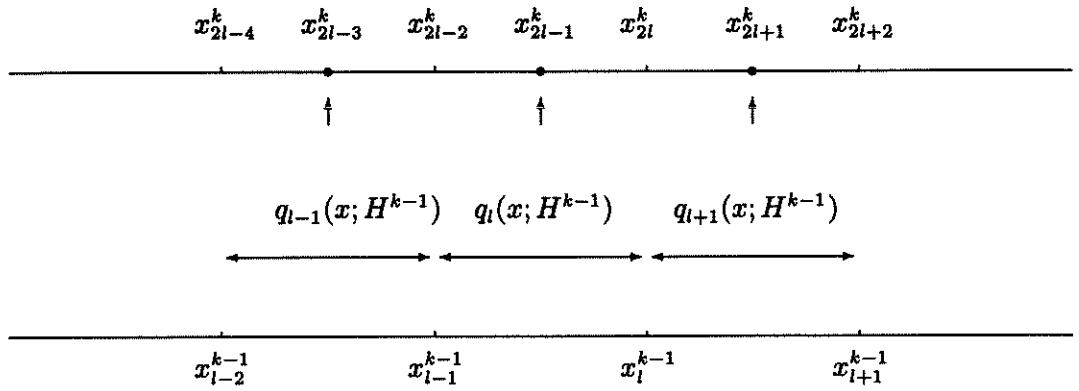

FIG. 1. *The polynomial pieces*

Let us consider the sequence of nested dyadic grids X^k of section 3 and assume that $x_d \in (x^{k-1}_{j-1}, x^{k-1}_j)$. We have then

$$\begin{aligned}\mathcal{R}^{SR}_{k-1}(x;\bar{f}^{k-1}) &= \frac{d^2}{dx^2} I^{SR}_{k-1}(x;H^{k-1}) \\ &= \tilde{I}^{SR}_{k-1}(x;H^{k-1}) + \sum_{\substack{i=1 \\ i\neq j-1,j}}^{J_{k-1}-1} s^{k-1}_i \delta(x-x^{k-1}_i) + \hat{s}^{k-1}_j \delta(x-\theta^{k-1}_j)\end{aligned}$$

where

$$\theta^{k-1}_j \in (x^{k-1}_{j-1}, x^{k-1}_j), \qquad G^{k-1}_j(\theta^{k-1}_j) = 0, \qquad G^{k-1}_j(x) = q^{k-1}_{j+1}(x;H^{k-1}) - q^{k-1}_{j-1}(x;H^{k-1}),$$

$$\tilde{I}^{SR}_{k-1}(x;H^{k-1}) = \begin{cases} \frac{d^2}{dx^2} q^{k-1}_l(x;H^{k-1}) & x \in [x^{k-1}_{l-1}, x^{k-1}_l]; \qquad l \neq j \\ \frac{d^2}{dx^2} q^{k-1}_{j-1}(x;H^{k-1}) & x \in [x^{k-1}_{j-1}, \theta^{k-1}_j] \\ \frac{d^2}{dx^2} q^{k-1}_{j+1}(x;H^{k-1}) & x \in [\theta^{k-1}_j, x^{k-1}_j] \end{cases}$$

and

$$\begin{aligned} s^{k-1}_l &= \left[\frac{d}{dx} q^{k-1}_{l+1}(x;H^{k-1}) - \frac{d}{dx} q^{k-1}_l(x;H^{k-1})\right]_{x^{k-1}_l} \qquad l \neq j-1, j, \\ \hat{s}^{k-1}_j &= \left[\frac{d}{dx} q^{k-1}_{j+1}(x;H^{k-1}) - \frac{d}{dx} q^{k-1}_{j-1}(x;H^{k-1})\right]_{x=\theta^{k-1}_j}. \end{aligned}$$

Hence,

$$\begin{aligned}(43) \quad (\hat{P}^k_{k-1}\bar{f}^{k-1})_l &= < \mathcal{R}^{SR}_{k-1}(x;\bar{f}^{k-1}), \omega^k_l > \\ &= < \tilde{I}^{SR}_{k-1}(x;H^{k-1}), \omega^k_l > + \sum_{\substack{i=1 \\ i\neq j-1,j}}^{J_{k-1}-1} s^{k-1}_i \omega^k_l(x^{k-1}_i) + \hat{s}^{k-1}_j \omega^k_l(\theta^{k-1}_j).\end{aligned}$$

Since $\mathrm{supp}(\omega^k_l) = [x^k_{l-1}, x^k_{l+1}]$, if $x^k_{l+1} \leq x^k_{2j-2} = x^{k-1}_{j-1}$ or $x^k_{l-1} \geq x^k_{2j} = x^{k-1}_j$ (i.e. $l \leq 2j-3$ or $l \geq 2j+1$) we can apply Lemma 6.2 in Part I to compute $< \tilde{I}^{SR}_{k-1}(x;\bar{f}^{k-1}), \omega^k_l >$. It is then

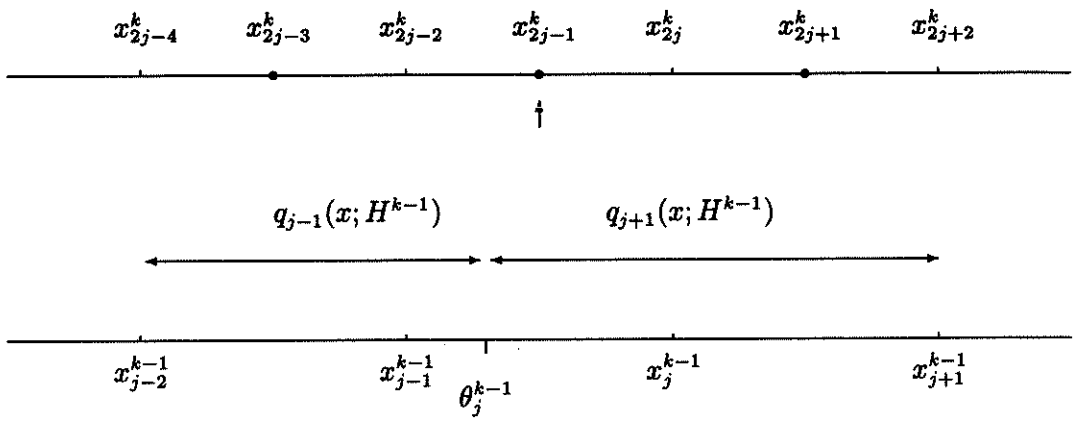

FIG. 2. *The polynomial pieces in SR*

easy to check that

$$< \tilde{I}^{SR}_{k-1}(x;\bar{f}^{k-1}),\omega^k_l > \;=\; \frac{1}{h_k}\left[(I^{SR}_{k-1})'(x^k_l-0;H^{k-1})-(I^{SR}_{k-1})'(x^k_l+0;H^{k-1})\right]+$$
$$\frac{1}{h^2_k}\left[I^{SR}_{k-1}(x^k_{l-1};H^{k-1})-2I^{SR}_{k-1}(x^k_l;H^{k-1})+I^{SR}_{k-1}(x^k_{l+1};H^{k-1})\right].$$

Hence,

$$< \mathcal{R}^{SR}_{k-1}(x;\bar{f}^{k-1}),\omega^k_l >=< \mathcal{R}_{k-1}(x;\bar{f}^{k-1}),\omega^k_l > \qquad l\neq 2j-2,2j-1,2j,$$

or, in other words,

$$(\hat{P}^k_{k-1}\bar{f}^{k-1})_l=(P^k_{k-1}\bar{f}^{k-1})_l \qquad l\neq 2j-2,2j-1,2j.$$

The local character of the SR technique implies thus that the prediction operator does not change outside of the area where the δ-singularity affects the sampled data.

In algorithms (34) and (35), only the predicted values at the odd-indexed grid points are computed. If

$$I_{k-1}(x;\tilde{\mathcal{D}}H)=q^{k-1}_l(x) \qquad x\in[x^{k-1}_{l-1},x^{k-1}_l]$$

then relation (33) becomes (see figure 1)

$$(P^k_{k-1}\bar{f}^{k-1})_{2l-1}=\frac{1}{h^2_k}\left[q^{k-1}_l(x^k_{2l-2})-2q^{k-1}_l(x^k_{2l-1})+q^{k-1}_l(x^k_{2l})\right].$$

Using the Newton form of the polynomial piece $q^{k-1}_l(x)$ and relation (26) it is easy to write $(P^k_{k-1}\bar{f}^{k-1})_{2l-1}$ in terms of $\{\bar{f}^{k-1}_i\}$ and their divided differences.

At a cell that contains a singularity, the SR technique modifies the polynomial pieces. A typical situation is depicted in figure 2. The computation of the predicted value at the middle point of the singular cell can be carried out from (43) by integration by parts. In the case displayed in figure 2, we obtain

$$\theta^{k-1}_j\in[x^k_{2j-2},x^k_{2j-1}] \qquad (\hat{P}^k_{k-1}\bar{f}^{k-1})_{2j-1}=\frac{1}{h^2_k}\left[q^{k-1}_{j+1}(x^k_{2j})-2q^{k-1}_{j+1}(x^k_{2j-1})+q^{k-1}_{j-1}(x^k_{2j-2})\right].$$

Also,

$$\theta_j^{k-1} \in [x_{2j-1}^k, x_{2j}^k] \qquad (\hat{P}_{k-1}^k \bar{f}^{k-1})_{2j-1} = \frac{1}{h_k^2}\left[q_{j+1}^{k-1}(x_{2j}^k) - 2q_{j-1}^{k-1}(x_{2j-1}^k) + q_{j-1}^{k-1}(x_{2j-2}^k)\right].$$

Even though we do not have the same polynomial piece on the right hand side of these expressions, it is not difficult to write either of them in terms of $\{\bar{f}_i^{k-1}\}$ and their divided differences. We assume that $\mathcal{S}_{j-1} \cap \mathcal{S}_{j+1} = \emptyset$; this should be the case if both stencils belong to the smooth part of the function. Then

$$q_{j-1}^{k-1}(x) = H(x_{j-1}^{k-1}) + H[x_{j-1}^{k-1}, x_{j-2}^{k-1}](x - x_{j-1}^{k-1}) + \sum_{m=3}^{r} H[x_{j-1}^{k-1}, \ldots, x_{j-m}^{k-1}](x - x_{j-1}^{k-1}) \cdots (x - x_{j-m+1}^{k-1}) \tag{44}$$

$$q_{j+1}^{k-1}(x) = H(x_j^{k-1}) + H[x_j^{k-1}, x_{j+1}^{k-1}](x - x_j^{k-1}) + \sum_{m=2}^{r-1} H[x_j^{k-1}, \ldots, x_{j+m}^{k-1}](x - x_j^{k-1}) \cdots (x - x_{j+m-1}^{k-1}) \tag{45}$$

Because of (26), the divided differences table constructed with the sampled values at a given resolution level, $\{\bar{f}^k\}$, can be related to the table of divided differences of $H(x)$ on that resolution level. In fact, if we define

$$\begin{cases} \bar{f}[x_i^k, x_{i+1}^k] = \frac{1}{h_k}\left(\bar{f}_{i+1}^k - \bar{f}_i^k\right) \\ \bar{f}[x_i^k, \ldots, x_{i+n}^k] = \frac{1}{nh_k}\left(\bar{f}[x_{i+1}^k, \ldots, x_{i+n}^k] - \bar{f}[x_i^k, \ldots, x_{i+n-1}^k]\right), \qquad n > 1 \end{cases}$$

it is easy to prove that

$$\bar{f}[x_i^k, \ldots, x_{i+n}^k] = (n+1)(n+2)H[x_{i-1}^k, \ldots, x_{i+n+1}^k]. \tag{46}$$

Thus, third and higher order divided differences in the expressions of $q_{j\pm1}^{k-1}$ can be directly expressed in terms of the sampled data. For instance, if $\theta_j^{k-1} \in [x_{2j-1}^k, x_{2j}^k]$ the right hand side of $(\hat{P}_{k-1}^k \bar{f}^{k-1})_{2j-1}$ can be expressed as

$$4\bar{f}_{j-1}^{k-1} - \frac{2}{h_k^2}\sum_{m=3}^{p+2} \frac{\bar{f}[x_{j-2}^{k-1}, \ldots, x_{j-m+1}^{k-1}]}{(m-1)(m-2)}(x_{2j-1}^k - x_{j-1}^{k-1}) \cdots (x_{2j-1}^k - x_{j-m+1}^{k-1})$$

An analogous expression, including only the sampled data at the $k-1$st level, can be found for $\theta_j^{k-1} \in [x_{2j-2}^k, x_{2j-1}^k]$.

To compute $(\hat{P}_{k-1}^k \bar{f}^{k-1})_{2j-1}$ it is not necessary to know the explicit location of the approximate singularity θ_j^{k-1}, only its relative location with respect to the grid point x_{2j-1}^k. In order to do this, it is enough to check the sign of

$$G_j^{k-1}(x_{2j-2}^k) \cdot G_j^{k-1}(x_{2j-1}^k).$$

Since second order (and higher) divided diferences of $H(x)$ can be written in terms of $\mathcal{D}f$ and its divided diferences, the function $G_j^{k-1} = q_{j+1}^{k-1}(x) - q_{j-1}^{k-1}(x)$ can also be expressed in terms of the samples $\bar{f}^{k-1}$ by re-arranging its lower order terms (LOT). Using (44) and (45) (and dropping the superindex notation), we get

$$\begin{aligned} LOT &= H(x_j) + H[x_j, x_{j+1}](x - x_j) - H(x_{j-1}) - H[x_{j-2}, x_{j-1}](x - x_{j-1}) \\ &= 2h^2 H[x_{j-2}, x_{j-1}, x_j] + (x - x_j)2h\{H[x_{j-2}, x_{j-1}, x_j] + H[x_{j-1}, x_j, x_{j+1}]\} \\ &= h^2 \bar{f}_{j-1} + (x - x_j)h\{\bar{f}_{j-1} + \bar{f}_j\}. \end{aligned}$$

5. Subcell Resolution at "Weaker" Singularities. As observed in section 2.2, the subcell resolution technique can also be applied to correct the reconstruction in cells that contain weaker singularities (jumps or corners in $f(x)$ for example, which correspond to discontinuities in H'' and H'''). However, one needs to be careful when applying the SR technique to these weak singularities.

Let $f(x) = g(x) + \alpha\delta(x - x_d)$, with $x_d \in (x_{j-1}, x_j)$ and $g(x)$ smooth; then its second primitive $H(x)$ has a corner at x_d. We observed in sections 2 and 4 that, when $\alpha = O(1)$, we can use the fact that $\mathcal{S}_{j-1} \cap \mathcal{S}_{j+1} = \emptyset$ to mark out those intervals suspected of containing a delta-type singularity.

In [5], one of us carries out a detailed analysis of the preferred form of the ENO interpolation process, the hierarchical form. This analysis reveals that Algorithm I might lead to a stencil selection such that $\mathcal{S}_{j-1} \cap \mathcal{S}_{j+1} \neq \emptyset$, when applied to a function $H(x)$ with a discontinuity in H'' (which would correspond to a jump in $f(x)$ itself). If this is the case, the interpolating polynomials next to the singularity may be constructed from a stencil that crosses the singularity. The accuracy of such polynomial pieces is thus degraded, and the SR technique has no chance to succeed.

In dealing with weak singularities, it becomes very important to isolate cells that are *suspected* of harboring a singularity. Once they are identified, the SR technique can be applied, provided we use accurate representations of the polynomial pieces to the left and to the right of the "singular" cell. This can be done by switching to Algorithm II, at those cells (see [5]).

The strategy then is as follows:

1. Sweep through the computational domain and calculate the ENO reconstruction at each cell using Algorithm I.

2. Use these reconstructions to single out cells suspected of harboring singularities.

REMARK 5.1. *The criterion*

$$\mathcal{S}_{j-1} \cap \mathcal{S}_{j+1} = \emptyset$$

indicates a possible discontinuity in $H'(x)$ within the j-th cell but cannot be used to detect weaker discontinuities. A more complete detection mechanism is outlined below.

3. Decide if the *suspicious* cell contains a singularity by using the G- function of the cell. If the check is positive, we label the cell as "singular".

3. If needed, re-compute the reconstructions at cells neighboring a "singular" cell to ensure that the stencil is chosen from the smooth part of the function. In other words, stencils corresponding to cells close to a "singular" cell should not *cross* that cell.

4. At each "singular" cell, modify the ENO reconstruction via SR, that is, extend the reconstructions to the left and to the right of the "singular" cell up to the computed location of the singularity.

These four steps are to be applied at the interpolation level, i.e. they should be applied to the second primitive in the hat-average setting, and to the first primitive in the cell-average multiresolution setting. In practice however, the strategy becomes again a design tool, and it can be carried out (as it should be) without explicit knowledge of the point values of $H(x)$. All that is required in the multiresolution schemes are the sampled values of the signal $f(x)$, that is $\mathcal{D}f$.

Here, we want to devise a strategy that will allow us to detect and identify discontinuities in H'' and H''' (jumps and corners in $f(x)$) and also *weak* δ-singularities, i.e. δ-type singularities where $\alpha = O(h_L)$ where L is the highest resolution level employed. We shall refer to these as "small δ". For these, Algorithm I can also lead to singularity-crossing stencils and to the failure of the plain SR technique.

When the singularity falls on a grid point, the basic ENO reconstruction procedure is not modified. However, we should point out that a *weak singularity* at the corner of a cell also needs to be identified. If $x_d = x_j$ is a δ singularity with $O(1)$ strength, then $\mathcal{S}_{j-1} \cap \mathcal{S}_j = \emptyset$ and all polynomial pieces have the desired accuracy. However, if $x_d = x_j$ is a *weak* singularity, Algorithm I might lead to singularity crossing stencils at the neighboring cells. To maintain the highest possible accuracy, the polynomial pieces next to a weak singularity should be recomputed using stencils that stay on a smooth side of the function.

To design a technique which will detect any of the aforementioned singularities, we had to consider at least the fourth order divided differences of $H(x)$. To make the notation easier we define

$$H[l;n] = H[x_l, x_{l+1}, \ldots, x_{l+n}]$$

Suppose we have a singularity at $x_d \in [x_{j-1}, x_j]$, say $x_d = x_j - ah$, $0 \le a \le 1$. Then the fourth order divided differences satisfy:

$$\begin{aligned}
H[j,4]) &= O(1) \\
H[j-1,4] &= \frac{1-a}{24h^3}[H']_d - \frac{(a-1)^2}{48h^2}[H'']_d - \frac{(a-1)^3}{144h}[H''']_d + O(1) \\
H[j-2,4] &= \frac{(3a-2)}{24h^3}[H']_d + \frac{3a^2-4a}{48h^2}[H'']_d + \frac{4-6a^2+3a^3}{144h}[H''']_d + O(1) \\
H[j-3,4] &= \frac{(1-3a)}{24h^3}[H']_d + \frac{1+2a-3a^2}{48h^2}[H'']_d + \frac{1+3a+3a^2-3a^3}{144h}[H''']_d + O(1) \\
H[j-4,4] &= \frac{a}{24h^3}[H']_d + \frac{a^2}{48h^2}[H'']_d + \frac{a^3}{144h}[H''']_d + O(1) \\
H[j-5,4] &= O(1).
\end{aligned}$$

We define (following the guidelines of [5])

$$\begin{aligned}
dci4(j) &:= \min\{|H[j-1,4]|, |H[j-2,4]|, |H[j-3,4]|, |H[j-4,4]|\} \\
dce4(j) &:= \min\{|H[j-1,4]|, |H[j-2,4]|, |H[j-3,4]|\} \\
dni4(j) &:= \max\{|H[j,4]|, |H[j-5,4]|\} \\
dne4(j) &:= \max\{|H[j,4]|, |H[j-4,4]|\}
\end{aligned}$$

The behavior of these quantities for the various *weak* singularities we want to detect is displayed in Tables 1 and 2.

case $x_d \in (x_{j-1}, x_j)$			
	delta	jump	corner
dci4(j)	$O(h_L/h^3)$	$O(1/h^2)$	$O(1/h)$
dni4(j)	$O(1)$	$O(1)$	$O(1)$
dce4(j)	$O(h_L/h^3)$	$O(1/h^2)$	$O(1/h)$
dne4(j)	$O(h_L/h^3)$	$O(1/h^2)$	$O(1/h)$

TABLE 1
divided differences of order 4

We then observe that

$$\begin{aligned}
x_d \in (x_{j-1}, x_j) &\Rightarrow dci4(j) > dni4(j) \\
x_d \approx x_j &\Rightarrow dce4(j) > dne4(j).
\end{aligned}$$

case $x_d \approx x_j$				case $x_d \approx x_{j-1}$			
	delta	jump	corner		delta	jump	corner
dci4(j)	$O(1)$	$O(1)$	$O(1)$	dci4(j-1)	$O(1)$	$O(1)$	$O(1)$
dni4(j)	$O(1)$	$O(1)$	$O(1)$	dni4(j-1)	$O(1)$	$O(1)$	$O(1)$
dce4(j)	$O(h_L/h^3)$	$O(1/h^2)$	$O(1/h)$	dce4(j-1)	$O(h_L/h^3)$	$O(1/h^2)$	$O(1/h)$
dne4(j)	$O(1)$	$O(1)$	$O(1)$	dne4(j-1)	$O(1)$	$O(1)$	$O(1)$

TABLE 2
divided differences of order 4

Then, if

$$dci4(j) > dni4(j) \tag{47}$$

we mark out the interval $[x_{j-1}, x_j]$ as suspected of having a singularity in its interior. On the other hand, if

$$dce4(j) > dne4(j) \tag{48}$$

we suspect a singularity at $x_d \approx x_j$

These criteria might fail in several cases. For instance, if we have a jump at x_j ($[H'']_{x_d} = O(1)$) and $[H''']_{x_j} = 0$, it turns out that $H[j-2,4] = O(1)$ and (48) is not true. Also, if $x_d = x_j - \frac{4}{3}h$ and $[H']_{x_d} = 0 = [H''']_{x_d}$, $[H'']_{x_d} = O(1)$, then $dci4(j) = O(1) = dni4(j)$ and (47) might fail.

To avoid these problematic cases, we analyze also the fifth order divided differences via Taylor expansions. It follows that the "exceptions" in the fourth-order divided differences are not correlated with the "exceptions" in the fifth order divided differences. We thus propose a detection algorithm that combines the information obtained from the fourth and fifth order divided differences. The final algorithm is given in the appendix.

One we have singled out the *suspicious* intervals, we must decide if they do indeed contain a singularity by using the function $G_j(x)$.

We know that when $H(x)$ has a discontinuity in its $m+1$st derivative at $x_d \in (x_{j-1}, x_j)$, it can be can approximated (for sufficiently small h) by the unique root of $G_j^{(m)}(z) = q_{j+1}^{(m)}(z) - q_{j-1}^{(m)}(z) = 0$. Thus, if (x_{j-1}, x_j) is suspected of containing a singularity, we check whether

$$G_j^{(m)}(x_{j-1}) \cdot G_j^{(m)}(x_j) < 0. \tag{49}$$

If this is the case, we conclude that there is a root of $G_j^{(m)}(z)$ in (x_{j-1}, x_j) and we proceed with the SR technique. Otherwise, no modifications are carried out on the basic ENO reconstruction. In practice we only try to identify δ-type singularities, jumps and corners in $f(x)$, thus we check (49) for $m = 0, 1, 2$.

A careful analysis of the functions $G_j^{(m)}(x)$ for $m = 0, 1, 2$ can help to determine whether or not a weak singularity lies at a *suspicious* grid point. This analysis is summarized in the appendix, together with our full detection mechanism.

6. Data Compression and Error Control. In this section we consider strategies for data compression and a priori bounds on the compression error.

The simplest data compression procedure is obtained by setting to zero all scale coefficients which fall below a prescribed tolerance. Let us denote

$$(\hat{d}^k)_j = \mathrm{tr}(d_j^k; \epsilon_k) = \begin{cases} 0 & |d_j^k| \le \epsilon_k \\ d_j^k & \text{otherwise} \end{cases} \tag{50}$$

and refer to this operation as truncation. This type of data compression is used primarily to reduce the "dimensionality" of the data. A different strategy, which is used to reduce the digital representation of the data for purposes of storage or transmission is "quantization" which can be modeled by

$$(\hat{d}^k)_j = \mathrm{qu}(d_j^k;\epsilon_k) = 2\epsilon_k \cdot \mathrm{round}\left[\frac{d_j^k}{2\epsilon_k}\right], \tag{51}$$

where round $[\cdot]$ denotes the integer obtained by rounding. For example, if $|d_j^k| \le 256$ and $\epsilon_k = 4$ then we can represent d_j^k by an integer which is not larger than 32 and commit a maximal error of 4. Observe that $|d_j^k| < \epsilon_k \Rightarrow \mathrm{qu}(d_j^k;\epsilon_k) = 0$ and that in both cases

$$|d_j^k - \mathrm{tr}(d_j^k;\epsilon_k)| \le \epsilon_k, \qquad |d_j^k - \mathrm{qu}(d_j^k;\epsilon_k)| \le \epsilon_k \tag{52}$$

Both strategies give us direct control over the rate of compression through an appropriate choice of the tolerance levels $\{\epsilon_k\}_{k=1}^L$. However once we use the values $\hat{d}_j^k$ in the corresponding decoding algorithm (4) we get an error which can often be estimated by analysis but cannot be directly controlled. The encoding-decoding strategy given by (3) and (4) is therefore suitable for applications where we are limited in capacity and we have to settle for whatever quality is possible under this limitation.

However, there are other applications where quality control is of utmost importance, yet we would like to be as economical as possible with respect to storage and speed of computation.

Given any tolerance level ϵ for accuracy, our task is to come up with a compressed representation

$$\{f^0, \hat{d}^1, \ldots, \hat{d}^L\} \tag{53}$$

such that

$$\| f^L - \hat{f}^L \|_\infty = \max_{1\le i\le N_L} |f_i^L - \hat{f}_i^L| \le C\epsilon \tag{54}$$

for $\hat{f}^L$ which is obtained by decoding the compressed multiresolution representation.

To accomplish this goal one can modify the encoding procedure along the following lines: For a predetermined decoding procedure, the modification allows us to keep track of the cumulative error and truncate accordingly. Given a tolerance level ϵ, the outcome of the modified encoding procedure should be a compressed representation (53) satisfying (54). This enables us to specify the desired level of accuracy in the decompressed signal. As to be expected (from considerations of the uncertainty principle), we cannot specify compression rate at the same time.

Modified encoding procedures for the interpolatory and cell-average frameworks can be found in [8]. In what follows, we describe a modification of the encoding technique within the hat-average framework, designed to monitor the cumulative compression error and truncate accordingly (for simplicity, we consider only truncation). We shall prove that, when used with the inverse multiresolution transform of the hat-average framework, the modification we propose satisfies (54).

The predetermined decoding procedure is (35). The algorithmic description of the modified encoding is as follows:

1. Compute the Multiresolution Analysis of the input data

$$\left\{\begin{array}{l} DO \quad k = L, 1 \\ \left\{\begin{array}{l} DO \quad j = 1, J_{k-1} - 1 \\ \bar{f}_j^{k-1} = \frac{1}{4}(\bar{f}_{2j-1}^k + 2\bar{f}_{2j}^k + \bar{f}_{2j+1}^k) \end{array}\right. \end{array}\right. \tag{55}$$

2. Set

$$\hat{f}^0 = \bar{f}^0 \tag{56}$$

3. Calculate

$$\left\{\begin{array}{l} DO \quad k = 1, L \\ \bar{f}_{J_k-1}^P = (P_{k-1}^k \hat{f}^{k-1})_{J_k-1} \\ \hat{d}_{J_{k-1}}^k = \mathrm{tr}(\bar{f}_{J_k-1}^k - \bar{f}_{J_k-1}^P, \epsilon_k) \\ \hat{f}_{J_k-1}^k = \bar{f}_{J_k-1}^P + \hat{d}_{J_{k-1}}^k \\ \left\{\begin{array}{l} DO \quad j = J_{k-1} - 1, 1, (-1) \\ \bar{f}_{2j-1}^P = (P_{k-1}^k \hat{f}^{k-1})_{2j-1} \\ \hat{d}_j^k = \mathrm{tr}([\bar{f}_{2j-1}^k - \bar{f}_{2j-1}^P] - [\bar{f}_j^{k-1} - \hat{f}_j^{k-1}], \epsilon_k) \\ \hat{f}_{2j-1}^k = \bar{f}_{2j-1}^P + \hat{d}_j^k \\ \hat{f}_{2j}^k = 2\hat{f}_j^{k-1} - \frac{1}{2}(\hat{f}_{2j-1}^k + \hat{f}_{2j+1}^k) \end{array}\right. \end{array}\right. \tag{57}$$

Let us denote the cumulative compression error at the k-th level by $\mathcal{E}_j^k$,

$$\mathcal{E}_j^k = \bar{f}_j^k - \hat{f}_j^k \tag{58}$$

and the prediction error by e_j^P,

$$e_j^P = \bar{f}_j^k - \bar{f}_j^P. \tag{59}$$

Let us prove that

$$|\mathcal{E}_{2j-1}^k| \leq \epsilon_k + \| \mathcal{E}^{k-1} \|_\infty, \quad \text{for } j = 1, \ldots, J_{k-1} \text{ and } \forall k. \tag{60}$$

Notice that for each $j = 1, \ldots, J_{k-1} - 1$,

$$\mathcal{E}_{2j-1}^k = e_{2j-1}^P - \mathrm{tr}(e_{2j-1}^P - \mathcal{E}_j^{k-1}, \epsilon_k), \tag{61}$$

Thus

$$\begin{array}{rcl} |e_{2j-1}^P - \mathcal{E}_j^{k-1}| > \epsilon_k & \Rightarrow & \mathcal{E}_{2j-1}^k = \mathcal{E}_j^{k-1}, \\ |e_{2j-1}^P - \mathcal{E}_j^{k-1}| \leq \epsilon_k & \Rightarrow & \mathcal{E}_{2j-1}^k = e_{2j-1}^P = e_{2j-1}^P - \mathcal{E}_j^{k-1} + \mathcal{E}_j^{k-1} \end{array}$$

In either case, we have

$$\mathcal{E}_{2j-1}^k = \rho_j^k + \mathcal{E}_j^{k-1} \qquad j = 1, \ldots, J_{k-1} - 1 \tag{62}$$

where

$$\rho_j^k = \left\{\begin{array}{ll} e_{2j-1}^P - \mathcal{E}_j^{k-1} & \text{if } |e_{2j-1}^P - \mathcal{E}_j^{k-1}| \leq \epsilon_k \\ 0 & \text{otherwise.} \end{array}\right.$$

Since

$$|\rho_j^k| \leq \epsilon_k \quad 1 \leq j \leq J_{k-1} - 1,$$

relation (60) follows from (62).

Expression (60) is also valid for $j = J_{k-1}$. In this case we have

$$\mathcal{E}_{J_k-1}^k = e_{J_k-1}^P - \mathrm{tr}(e_{J_k-1}^P, \epsilon_k).$$

Thus,

$$\begin{aligned} |e_{J_k-1}^P| &> \epsilon_k \Rightarrow |\mathcal{E}_{J_k-1}^k| = 0 \\ |e_{J_k-1}^P| &\leq \epsilon_k \Rightarrow |\mathcal{E}_{J_k-1}^k| = |e_{J_k-1}^P| \leq \epsilon_k. \end{aligned}$$

In other words,

$$\mathcal{E}_{J_k-1}^k = \rho_{J_k-1}^k = \begin{cases} 0 & \text{if } |e_{J_k-1}^P| > \epsilon_k \\ e_{J_k-1}^P & \text{otherwise.} \end{cases} \tag{63}$$

Now, (60) follows from the fact that $|\rho_{J_k-1}^k| < \epsilon_k$.

Let us prove now that

$$|\mathcal{E}_{2j}^k| \leq \epsilon_k + 2 \parallel \mathcal{E}^{k-1} \parallel_\infty, \quad j = 1, \ldots, J_{k-1} - 1. \tag{64}$$

It is easy to check that

$$\mathcal{E}_{2j}^k = 2\mathcal{E}_j^{k-1} - \frac{1}{2}(\mathcal{E}_{2j-1}^k + \mathcal{E}_{2j+1}^k), \qquad 1 \leq j \leq J_{k-1} - 1. \tag{65}$$

Thus, using (62)

$$\begin{aligned} \mathcal{E}_{2j}^k &= 2\mathcal{E}_j^{k-1} - \frac{1}{2}[\rho_{j+1}^k + \mathcal{E}_{j+1}^{k-1} + \rho_j^k + \mathcal{E}_j^k] \\ &= \frac{3}{2}\mathcal{E}_j^{k-1} - \frac{1}{2}\mathcal{E}_{i+1}^{k-1} - \frac{1}{2}[\rho_{j+1}^k + \rho_j^k]. \end{aligned}$$

for $1 \leq j \leq J_{k-1} - 2$. Therefore

$$|\mathcal{E}_{2j}^k| \leq \frac{3}{2}|\mathcal{E}_j^{k-1}| + \frac{1}{2}|\mathcal{E}_{i+1}^{k-1}| + \frac{1}{2}[\epsilon_k + \epsilon_k] \leq 2||\mathcal{E}||_\infty + \epsilon_k \qquad 1 \leq j \leq J_{k-1} - 2. \tag{66}$$

Analogously, using (65) and (63) we obtain

$$|\mathcal{E}_{J_k-2}| \leq \frac{3}{2}|\mathcal{E}_{J_{k-1}-1}^{k-1}| + \epsilon_k \leq 2||\mathcal{E}||_\infty + \epsilon_k.$$

Recalling that $\mathcal{E}^0 = 0$, we get from (60) and (64)

$$\parallel \mathcal{E}^L \parallel_\infty \leq \epsilon_L + 2 \parallel \mathcal{E}^{L-1} \parallel_\infty \leq \ldots \leq \sum_{l=1}^{L} 2^{L-l}\epsilon_l; \tag{67}$$

hence, taking

$$\epsilon_l = \epsilon \cdot q^{L-l} \qquad 0 < q \leq \frac{1}{2} \tag{68}$$

we get

$$\| \bar{f}^L - \hat{f}^L \|_\infty = \| \mathcal{E}^L \|_\infty \leq \begin{cases} (1-2q)^{-1}\epsilon & 0 < q < 1/2 \\ L\epsilon & q = 1/2 \end{cases} \tag{69}$$

We can also derive a priori bounds for the l_1 error. We define

$$||\mathcal{E}^k||_1 = h_k \sum_{i=1}^{J_k - 1} |\mathcal{E}_i^k|.$$

Thus

$$||\mathcal{E}^k||_1 = h_k \{ |\mathcal{E}_{J_k-1}^k| + \sum_{i=1}^{J_{k-1}-1} [|\mathcal{E}_{2i-1}^k| + |\mathcal{E}_{2i}^k|] \}. \tag{70}$$

Notice that

$$\begin{aligned} \mathcal{E}_{2i}^k + \mathcal{E}_{2i-1}^k &= 2\mathcal{E}_i^{k-1} + \frac{1}{2}\mathcal{E}_{2i-1}^k - \frac{1}{2}\mathcal{E}_{2i+1}^k \\ \mathcal{E}_{2i}^k - \mathcal{E}_{2i-1}^k &= 2\mathcal{E}_i^{k-1} - \frac{3}{2}\mathcal{E}_{2i-1}^k - \frac{1}{2}\mathcal{E}_{2i+1}^k. \end{aligned}$$

Then

$$\begin{aligned} |\mathcal{E}_{2i}^k| + |\mathcal{E}_{2i-1}^k| &= \max(|\mathcal{E}_{2i}^k + \mathcal{E}_{2i-1}^k|, |\mathcal{E}_{2i}^k - \mathcal{E}_{2i-1}^k|) \\ &\leq 2|\mathcal{E}_i^{k-1}| + \frac{3}{2}|\mathcal{E}_{2i-1}^k| + \frac{1}{2}|\mathcal{E}_{2i+1}^k| \end{aligned}$$

and

$$\begin{aligned} \sum_{i=1}^{J_{k-1}-1} [|\mathcal{E}_{2i-1}^k| + |\mathcal{E}_{2i}|] &= \sum_{i=1}^{J_{k-1}-1} 2|\mathcal{E}_i^{k-1}| + \frac{3}{2}|\mathcal{E}_{2i-1}^k| + \frac{1}{2}|\mathcal{E}_{2i+1}^k| \\ &\leq 2\sum_{i=1}^{J_{k-1}-1} |\mathcal{E}_i^{k-1}| + 2\sum_{i=1}^{J_{k-1}-1} |\mathcal{E}_{2i-1}^k| + \frac{1}{2}|\mathcal{E}_{J_k-1}^k|. \end{aligned}$$

Substituting in (70) and taking into account (62) and (63) we get

$$||\mathcal{E}^k||_1 \leq \frac{h_{k-1}}{2} \left\{ 2\sum_{i=1}^{J_{k-1}-1} |\mathcal{E}_i^{k-1}| + \epsilon_k(2J_{k-1} - 2 + \frac{3}{2}) \right\} \leq 2||\mathcal{E}^{k-1}||_1 + \epsilon_k,$$

and we obtain the same bounds as in the $||\cdot||_\infty$ case provided $||\mathcal{E}^0||_1 = 0$.

If the reconstruction operators $\mathcal{R}_k$ are linear functionals, the error-control technique we have described allows us to control the quality of the decoded data instead of the compression rate. If the reconstruction operators are non linear (data dependent) this algorithm guarantees the stability of the data compression procedure, while a simpler algorithm like (34), (35) does not.

7. Numerical Experiments. In this section, we carry out several experiments to test the performance of various compression algorithms and compare their results.

In all our experiments the finest grid X^L is a uniform grid of $J_L = 1024$ points. The multiresolution schemes are used with 7 levels of resolution, i.e. $L = 7$ and $J_0 = 8$. The scale coefficients are truncated by (50).

The linear schemes we consider are the following:

1. Daubechies orthonormal wavelets.
2. The piecewise polynomial reconstruction of Part I [3] using a periodic extension at the boundary. We proved in [3] that these schemes are the same as the Biorthogonal wavelets of [4] with the hat-function as the mother scaling function ($\tilde{N} = 2$ in the notation of [4]).
3. The piecewise polynomial reconstruction of Part I [3] with one-sided stencils at the boundaries.

The nonlinear schemes are based on the ENO and ENO-SR reconstruction procedures described in sections 4 and 5.

The truncation strategy, that is the choice of ϵ_k, varies with the type of reconstruction. For linear schemes, we use $\epsilon_k = \epsilon$, $\forall k$ and the un-modified encoding algorithm. In the non-linear case we need to use the modified encoding algorithm of section 6. In this case, our choice is $\epsilon_k = \epsilon/2^{L-k+1}$ which ensures (see (67)) that $||\mathcal{E}^L||_{1,\infty} \leq L\epsilon/2$. We also explore the influence of other strategies in the linear and non-linear cases.

In our first set of experiments, we consider a signal that exhibits a particular type of singularity.
The *kink function*

$$f_1(x) = |\sin(\frac{3}{2}\pi(x - \frac{1}{2}))| \qquad x \in [0,1] \tag{71}$$

The *step function*

$$f_2(x) = \begin{cases} \frac{1}{2}\sin(\pi x) & x \leq \frac{2}{3} \\ \frac{1}{2} - \sin(\pi x) & x > \frac{2}{3} \end{cases} \tag{72}$$

The *δ-function*

$$f_3(x) = \sin(\frac{\pi}{4}x) + \delta(x - x_{741}) + \frac{1}{1024}\delta(x - x_{241}) \tag{73}$$

Discrete data is obtained by considering point-values of $f_1(x)$ and $f_2(x)$ on the grid X^L; the discrete data associated to $f_3(x)$ are also its point-values on the grid X^L except for $\bar{f}_{241} = \sin(\frac{\pi}{4}x_{241}) + 1$ and $\bar{f}_{741} = \sin(\frac{\pi}{4}x_{741}) + 1024$. The discrete data are displayed in the leftmost corner of figures 3, 4 and 5 (for $f_3(x)$, only the smooth part and the small δ are displayed).

In the aforementioned figures, and for each multiresolution scheme considered, we also display the location of the scale coefficients that are different from zero after the truncation process has taken place. We do so by drawing a circle around (ξ^k, k) where $\xi^k = (j - \frac{1}{2})h_k$, $h_k = 2^{L-k}h_L$ for each d_j^k which is above the tolerance ϵ_k.

Tables 3, 4 and 5 display the order of the reconstruction procedure that defines the multiresolution scheme (we refer to the order as p), the compression factor, computed as

$$\text{Compression} = \frac{\text{number of elements in } \bar{f}^L}{\text{number of non-zero elements in } \hat{f}^L},$$

the errors (between the original and reconstructed signals) $||\mathcal{E}^L||_\infty$ and $||\mathcal{E}^L||_1$ and the choice of ϵ_k.

In the sets of figures 3, 4 and 5 we observe that the smooth part of the data is resolved to the prescribed tolerance at level 2. The significant scale-coefficients in levels 3 to 7 are the *signature* of the singularities for each prediction operator. In the wavelet case (orthonormal

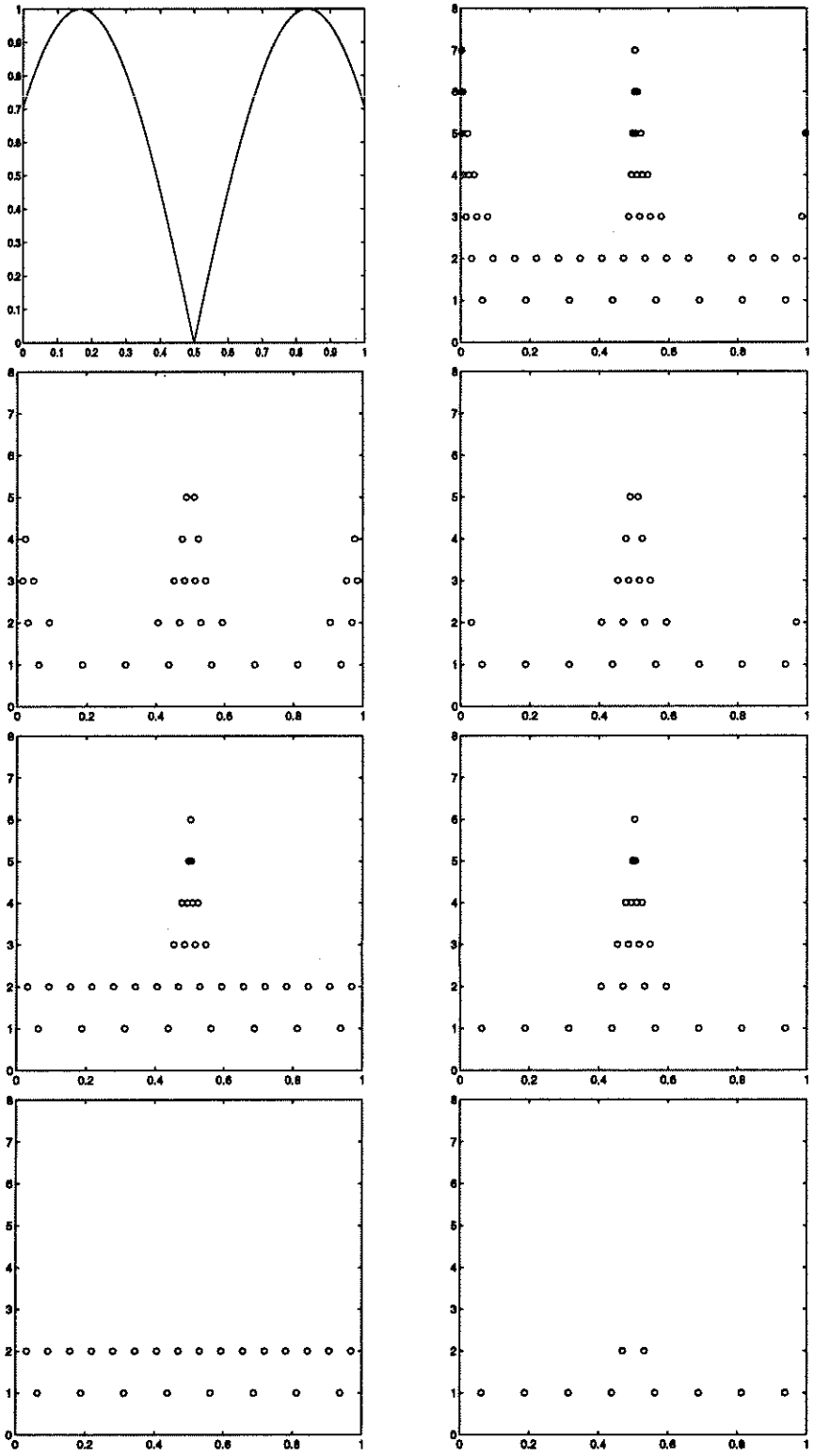

FIG. 3. . *Top to bottom and left to right: kink function, O-4;BO-4, PP-4; ENO-4, ENO-5; ENO-SR-4, ENO-SR-5*

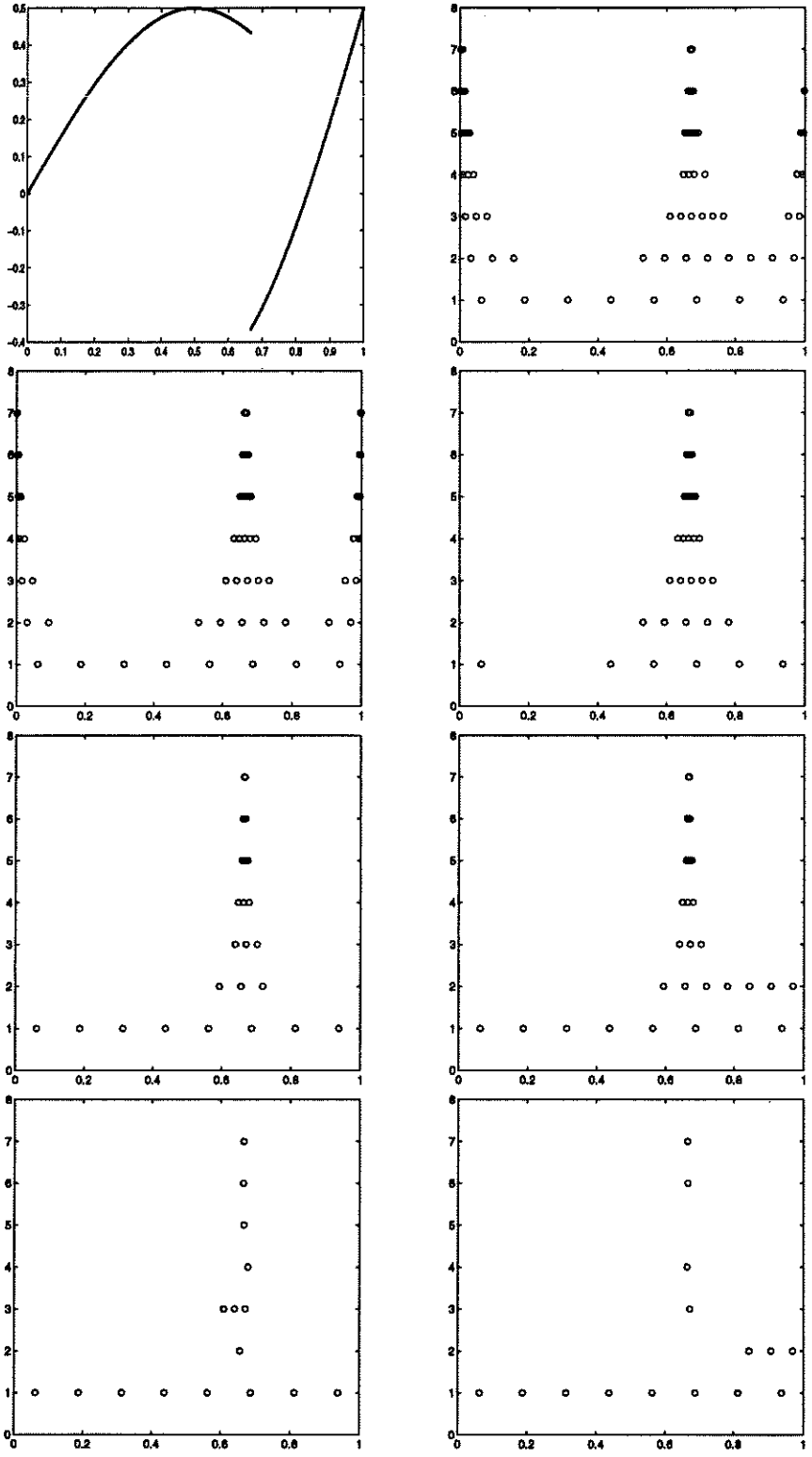

FIG. 4. . *Top to bottom and left to right: step function, O-4;BO-4, PP-4; ENO-4, ENO-5; ENO-SR-4, ENO-SR-5*

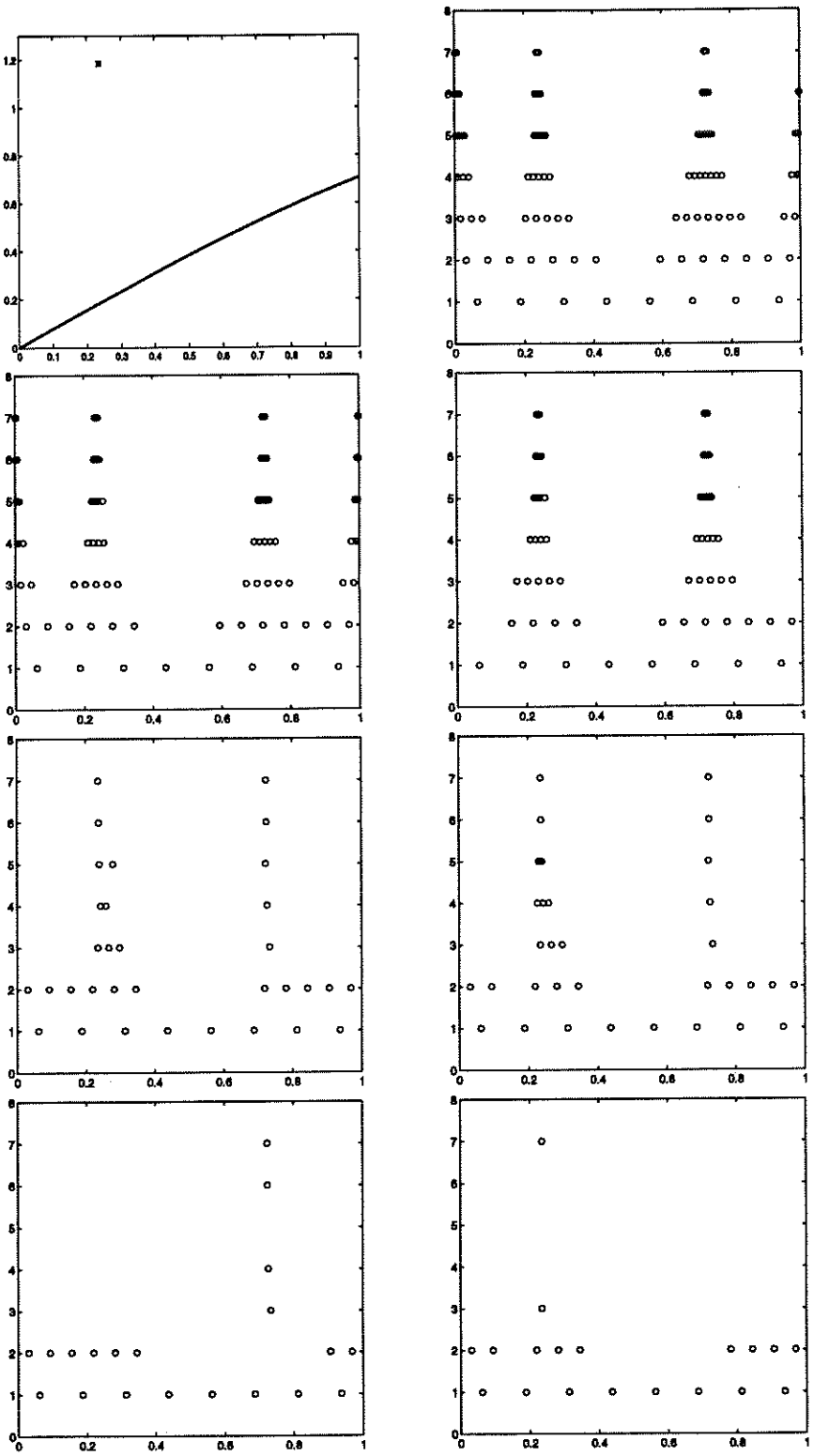

FIG. 5. . *Top to bottom and left to right: δ function, O-4;BO-4, PP-4; ENO-4, ENO-5; ENO-SR-4, ENO-SR-5*

Method	Order	Compression	L_∞-error	L_1-error	ϵ_k
Orthonormal wavelets	4	19.69	$5.24 \cdot 10^{-4}$	$2.91 \cdot 10^{-5}$	.001
Biorthogonal wavelets	4	26.95	$2.50 \cdot 10^{-3}$	$2.56 \cdot 10^{-4}$	.001
Piecewise polynomial	4	34.10	$2.35 \cdot 10^{-3}$	$3.18 \cdot 10^{-4}$	.001
ENO reconstruction	4	23.79	$5.36 \cdot 10^{-3}$	$6.80 \cdot 10^{-5}$	$.01/2^{L-k+1}$
ENO reconstruction	5	33.00	$4.77 \cdot 10^{-3}$	$3.95 \cdot 10^{-5}$	$.01/2^{L-k+1}$
ENO-SR reconstruction	4	31.99	$3.50 \cdot 10^{-3}$	$3.77 \cdot 10^{-5}$	$.01/2^{L-k+1}$
ENO-SR reconstruction	5	56.83	$8.80 \cdot 10^{-3}$	$4.25 \cdot 10^{-5}$	$.01/2^{L-k+1}$

TABLE 3
kink-function

Method	Order	Compression	L_∞-error	L_1-error	ϵ_k
Orthonormal wavelets	4	13.65	$2.89 \cdot 10^{-4}$	$1.36 \cdot 10^{-5}$	.001
Biorthogonal wavelets	4	15.05	$8.86 \cdot 10^{-4}$	$7.86 \cdot 10^{-5}$	.001
Piecewise polynomial	4	23.79	$2.82 \cdot 10^{-3}$	$2.09 \cdot 10^{-4}$	.001
ENO reconstruction	4	31.00	$7.64 \cdot 10^{-4}$	$3.68 \cdot 10^{-5}$	$.01/2^{L-k+1}$
ENO reconstruction	5	27.65	$8.47 \cdot 10^{-5}$	$2.73 \cdot 10^{-6}$	$.01/2^{L-k+1}$
ENO-SR reconstruction	4	42.62	$4.27 \cdot 10^{-3}$	$9.66 \cdot 10^{-5}$	$.01/2^{L-k+1}$
ENO-SR reconstruction	5	44.48	$4.94 \cdot 10^{-3}$	$3.64 \cdot 10^{-5}$	$.01/2^{L-k+1}$

TABLE 4
step-function

Method	Order	Compression	L_∞-error	L_1-error	ϵ_k
Orthonormal wavelets	4	9.57	$3.34 \cdot 10^{-4}$	$1.70 \cdot 10^{-5}$	.001
Biorthogonal wavelets	4	10.56	$2.02 \cdot 10^{-3}$	$2.05 \cdot 10^{-5}$	.001
Piecewise polynomial	4	13.64	$2.07 \cdot 10^{-3}$	$1.24 \cdot 10^{-4}$	.001
ENO reconstruction	4	24.95	$3.30 \cdot 10^{-3}$	$2.19 \cdot 10^{-5}$	$.01/2^{L-k+1}$
ENO reconstruction	5	24.95	$5.28 \cdot 10^{-3}$	$5.34 \cdot 10^{-5}$	$.01/2^{L-k+1}$
ENO-SR reconstruction	4	36.53	$2.08 \cdot 10^{-3}$	$1.41 \cdot 10^{-5}$	$.01/2^{L-k+1}$
ENO-SR reconstruction	5	37.89	$5.45 \cdot 10^{-3}$	$2.60 \cdot 10^{-5}$	$.01/2^{L-k+1}$

TABLE 5
δ-function

and biorthogonal) we also get the *signature* of the singularity introduced at the boundary by the periodicity assumption.

In each figure, O stands for 'Orthonormal wavelets'; BO for Biorthogonal wavelets; PP for the piecewise polynomial reconstruction described in [3] with one-sided reconstructions at the boundary. The ENO labels are self explanatory. The order of the reconstruction procedure follows the scheme identification name, for example O-4 stands for Orthonormal wavelets of order 4 (4 vanishing moments). The truncation strategy is as specified in tables 3, 4 and 5.

Biorthogonal wavelets give a better compression rate than orthogonal wavelets; their *signature* appears to be slightly narrower. In addition, removing the periodicity assumption, i.e. using the piecewise polynomial reconstruction procedures of [3] with one-sided stencils at the boundaries, leads to larger compression rates, since the *signature* of the boundary is basically eliminated.

As observed in section 5, the ENO reconstruction is fooled by the weak singularities (the corner, jump and *small* δ), while it isolates perfectly the $O(1)$ δ in $f_3(x)$. The addition of

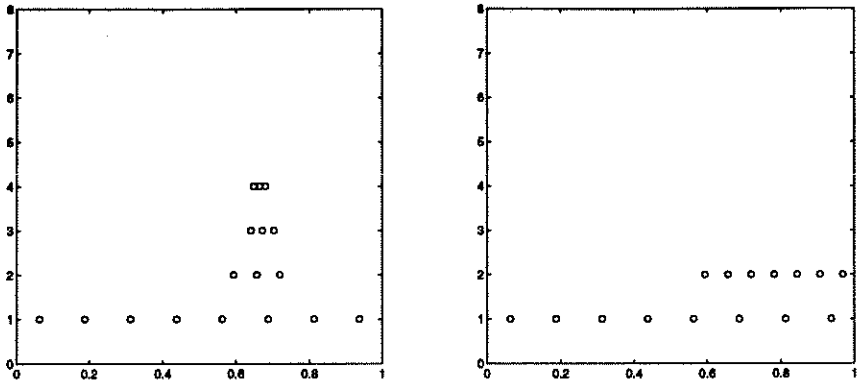

FIG. 6. *Step-function; left ENO-SR-4 SR only up to level 5; right ENO-SR-5 SR only up to level 3*

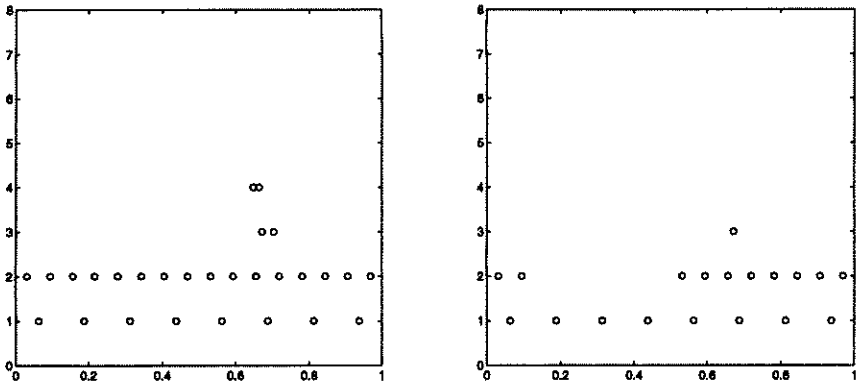

FIG. 7. *Step-function; left ENO-SR-4; right ENO-SR-5* $\epsilon_k = \epsilon/4^{L-k+1}$

the SR technique improves the compression rate and sometimes does eliminate completely the signature of each singularity.

We observe that the ENO+SR technique attains the largest compression rate, while (thanks to the modified encoding algorithm) keeping the error below the specified tolerance (in this case ϵ_L).

In figure 3 the singularity is located at the center of the computational domain. The influence of the one-sided reconstructions at the boundary is not felt until the coarsest level is attained, and the SR technique is very effective. The pattern of non-zero elements is about the same in all the weak singularities we study, if their initial location in the finest grid is the same.

To observe the boundary effects, we have located the jump discontinuity in $f_2(x)$ closer to the right boundary. Figure 4 shows the pattern of non-zero scale coefficients in this case. We see that the one sided reconstruction procedures, together with the truncation strategy imposed by the modified encoding algorithm, leads to a non-empty signature at the discontinuity even when applying the SR technique. We have observed that our detection mechanism always locates the singularity, but the approximation properties of the one-sided reconstructions might not be good enough to eliminate completely the signature in the coarsest levels. The (highly localized) perturbations are then carried back to the higher resolution levels by the modified encoding algorithm.

Since this framework allows us to choose a different reconstruction technique at each resolution level, we can apply the SR technique only up to a certain level. For the step-

Method	Order	Compression	L_∞-error	L_1-error	ϵ_k
Orthonormal wavelets	4	17.96	$1.63 \cdot 10^{-3}$	$2.81 \cdot 10^{-5}$	$.01/2^{L-k+1}$
Biorthogonal wavelets	4	22.26	$2.50 \cdot 10^{-3}$	$7.80 \cdot 10^{-5}$	$.01/2^{L-k+1}$
Piecewise polynomial	4	25.57	$2.25 \cdot 10^{-3}$	$5.30 \cdot 10^{-5}$	$.01/2^{L-k+1}$
ENO reconstruction	4	14.41	$8.55 \cdot 10^{-4}$	$9.90 \cdot 10^{-5}$	$.01/4^{L-k+1}$
ENO reconstruction	5	22.73	$4.17 \cdot 10^{-4}$	$4.86 \cdot 10^{-6}$	$.01/4^{L-k+1}$
ENO-SR reconstruction	4	17.05	$7.37 \cdot 10^{-5}$	$3.26 \cdot 10^{-6}$	$.01/4^{L-k+1}$
ENO-SR reconstruction	5	34.10	$5.40 \cdot 10^{-4}$	$2.33 \cdot 10^{-6}$	$.01/4^{L-k+1}$
ENO-SR reconstruction	6	31.00	$9.52 \cdot 10^{-4}$	$4.08 \cdot 10^{-6}$	$.01/4^{L-k+1}$

TABLE 6
kink-function ϵ_k-strategies

Method	Order	Compression	L_∞-error	L_1-error	ϵ_k
Orthonormal wavelets	4	13.65	$5.61 \cdot 10^{-4}$	$1.31 \cdot 10^{-5}$	$.01/2^{L-k+1}$
Biorthogonal wavelets	4	14.84	$9.86 \cdot 10^{-5}$	$1.54 \cdot 10^{-5}$	$.01/2^{L-k+1}$
Piecewise polynomial	4	22.73	$4.29 \cdot 10^{-4}$	$2.99 \cdot 10^{-5}$	$.01/2^{L-k+1}$
ENO reconstruction	4	22.24	$3.57 \cdot 10^{-5}$	$2.40 \cdot 10^{-6}$	$.01/4^{L-k+1}$
ENO reconstruction	5	26.23	$3.12 \cdot 10^{-5}$	$1.15 \cdot 10^{-6}$	$.01/4^{L-k+1}$
ENO-SR reconstruction	4	28.42	$4.42 \cdot 10^{-4}$	$4.30 \cdot 10^{-6}$	$.01/4^{L-k+1}$
ENO-SR reconstruction	5	37.89	$1.96 \cdot 10^{-3}$	$5.29 \cdot 10^{-6}$	$.01/4^{L-k+1}$
ENO-SR reconstruction	6	42.62	$3.28 \cdot 10^{-4}$	$1.41 \cdot 10^{-6}$	$.01/4^{L-k+1}$

TABLE 7
step-function ϵ_k-strategies

function, we can obtain absolute compression up to level 4 for $p = 4$ and up to level 2 for $p = 5$ (see figure 6); however, the compression rate and the errors are basically unchanged.

In figure 5 we superimpose two δ-functions of different strength to an underlying smooth signal. We observe a difference in the way the ENO technique deals with the $O(1)$ and $O(h_L)$ δ-singularities. The signature of the $O(1)$-δ is just one point, but the *small* δ does fool the hierarchical stencil selection algorithm producing poorer approximations and, in turn, a wider signature than in the $O(1)$ case. As before, the non-empty signature in the SR-case is a result of the proximity of the singularity to the boundary. It can also be eliminated by applying the SR technique on a limited number of levels (starting from the finest).

Notice that the signature of either singularity in any of the linear schemes is always larger than in the non-linear schemes.

Tables 6, 7 and 8 display the compression rate and the error for a different truncation strategy. Comparing the results in these tables with those of tables 3, 4 and 5 we make the following observations:

1. For linear schemes, the $\epsilon_k = \epsilon$ and $\epsilon_k = \epsilon/2^{L-k+1}$ strategies lead to essentially the same results. The errors in tables 6, 7 and 8 are slightly smaller than those in tables 3, 4 and 5, but the corresponding compression rate is slightly smaller too. Similar results could be obtained by increasing ϵ in the $\epsilon_k = \epsilon$ strategy.
2. For non-linear schemes, the strategy $\epsilon_k = \epsilon/2^{L-k+1}$ always leads to numerical errors which are smaller than ϵ, although the theoretical bound is $L\epsilon/2$. A strategy like $\epsilon_k = \epsilon/4^{L-k+1}$ leads to a moderate decrease in the compression rate and an improvement (of more than an order of magnitude) in the numerical error. It also improves the effectiveness of the SR technique (see figure 7).

Method	Order	Compression	L_∞-error	L_1-error	ϵ_k
Orthonormal wavelets	4	9.39	$3.43 \cdot 10^{-4}$	$6.87 \cdot 10^{-6}$	$.01/2^{L-k+1}$
Biorthogonal wavelets	4	10.56	$2.02 \cdot 10^{-3}$	$2.05 \cdot 10^{-5}$	$.01/2^{L-k+1}$
Piecewise polynomial	4	13.29	$2.02 \cdot 10^{-3}$	$2.05 \cdot 10^{-5}$	$.01/2^{L-k+1}$
ENO reconstruction	4	24.95	$2.45 \cdot 10^{-5}$	$1.75 \cdot 10^{-7}$	$.01/4^{L-k+1}$
ENO reconstruction	5	24.95	$3.45 \cdot 10^{-6}$	$1.81 \cdot 10^{-8}$	$.01/4^{L-k+1}$
ENO-SR reconstruction	4	37.89	$3.51 \cdot 10^{-4}$	$8.14 \cdot 10^{-7}$	$.01/4^{L-k+1}$
ENO-SR reconstruction	5	39.35	$2.27 \cdot 10^{-4}$	$5.49 \cdot 10^{-7}$	$.01/4^{L-k+1}$
ENO-SR reconstruction	6	39.35	$6.05 \cdot 10^{-6}$	$1.22 \cdot 10^{-8}$	$.01/4^{L-k+1}$

TABLE 8
δ-function ϵ_k-strategies

Method	Order	Compression	L_∞-error	L_1-error	ϵ_k
Orthonormal wavelets	4	6.65	$3.423 \cdot 10^{-4}$	$2.896 \cdot 10^{-5}$	.001
Biorthogonal wavelets	4	7.94	$2.148 \cdot 10^{-3}$	$2.512 \cdot 10^{-4}$	.001
Piecewise polynomial	4	9.23	$1.460 \cdot 10^{-2}$	$3.524 \cdot 10^{-4}$	.001
ENO reconstruction	4	10.14	$4.388 \cdot 10^{-3}$	$1.188 \cdot 10^{-4}$	$.01/2^{L-k+1}$
ENO reconstruction	5	10.45	$3.359 \cdot 10^{-3}$	$7.711 \cdot 10^{-5}$	$.01/2^{L-k+1}$
ENO-SR reconstruction	4	13.65	$4.846 \cdot 10^{-3}$	$2.053 \cdot 10^{-4}$	$.01/2^{L-k+1}$
ENO-SR reconstruction	5	15.75	$4.860 \cdot 10^{-3}$	$8.376 \cdot 10^{-5}$	$.01/2^{L-k+1}$

TABLE 9
Harten's function

To finish, we consider Harten's function, with the addition of a *small* δ,

$$f_4(x) = \frac{1}{1024}\delta(x - x_{865}) + \begin{cases} -x\sin(\frac{3\pi}{2}x^2) & -1 < x \le -\frac{1}{3} \\ |\sin(2\pi x)| & |x| < \frac{1}{3} \\ 2x - 1 - \sin(3\pi x)/6 & \frac{1}{3} \le x < 1. \end{cases}$$

Figure 8 displays the discrete input data and the pattern of non-zero scale coefficients corresponding to the numerical experiments in table 9.

The number of singularities present in this function make it an interesting test for compression methods. As before, the ENO-SR method attains the highest compression rate while keeping the error below the specified tolerance.

8. Summary and Conclusions. In [8, 9, 10], A. Harten introduces a general framework for multiresolution schemes based on two operators: Decimation (always linear) and Prediction (linear or non linear).

In [3] and this paper we consider the decimation operator which is derived from the discretization process of taking local averages with respect to the hat function.

In the first paper in the series, [3], we considered linear prediction operators based on centered interpolation and studied the stability properties of the resulting multiresolution schemes. Here we consider non-linear prediction operators based on ENO interpolation. We design a modified encoding algorithm whithin the hat-weighted framework that keeps track of the cumulative error and leads to stable multiresolution schemes even for non-linear prediction operators.

In the hat-multiresolution context, the ENO technique allows us to detect δ-type singularities, one can then use Harten's Subcell Resolution technique to improve the accuracy

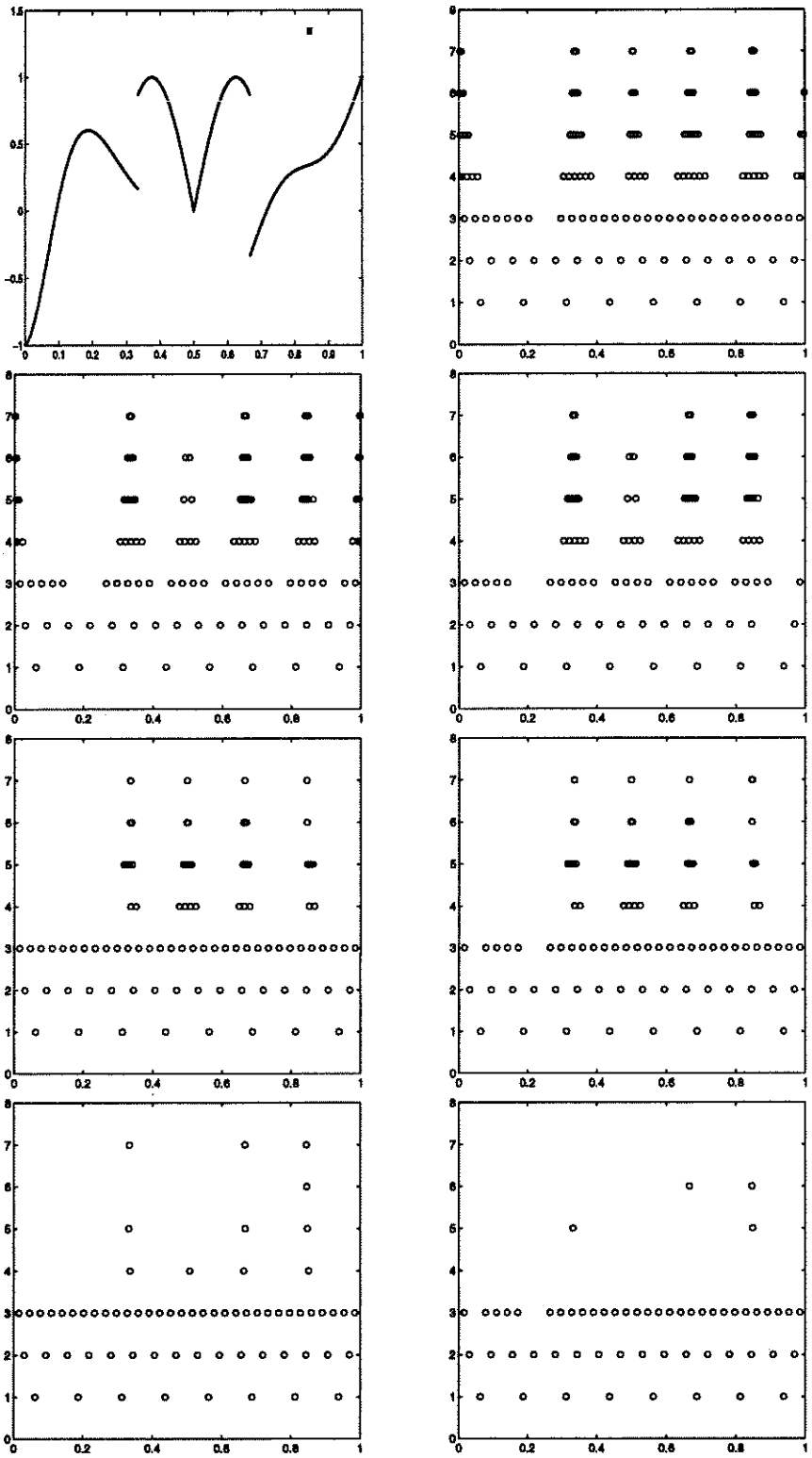

FIG. 8. . *Top to bottom and left to right: Harten's function, O-4;BO-4, PP-4; ENO-4, ENO-5; ENO-SR-4, ENO-SR-5*

of the prediction. We also design a more elaborate detection mechanism that allows us to apply the SR technique to jump-discontinuities and to discontinuities in the derivative of the original signal (corners).

Our numerical experiments confirm our theoretical observations: the non-linear schemes always give higher compression rates than the linear ones. Highest compression occurs at resolution levels for which the singularities are well separated, i.e. it is possible to choose a stencil for the interpolating polynomials that stays within a region of smoothness of the original signal.

REFERENCES

[1] R. Abgrall, *Design of an Essentially Nonoscillatory Reconstruction Procedure on Finite Element Type Meshes*, FEbruary 1992, ICASE Report 91-84, December 1991, revised INRIA report 1592; also Math. Comp. submitted.

[2] R. Abgrall, A. Harten *Multiresolution Representation in Structured Meshes. I Preliminary Report*, UCLA CAM Report 94-20 (1994)

[3] F.Aràndiga, R. Donat and A. Harten, *Multiresolution Based on Weighted Averages of the Hat Function I: Linear Reconstruction Operators*, UCLA CAM Report 96-25

[4] A. Cohen, I. Daubechies and J.C. Feauveau, *Biorthogonal Bases of Compactly Supported Wavelets*, Comm. Pure Applied Math., **45** (1992), pp. 485-560.

[5] R. Donat *Studies on Error Propagation for Certain Nonlinear Approximations to Hyperbolic Equations: Discontinuities in Derivatives*, SINUM, **31** (1994) pp. 655-679.

[6] R. Donat and A. Harten, *Data Compression Algorithms for Locally Oscilatory Data*, UCLA CAM Report 93-26 (1993)

[7] A. Harten, *ENO Schemes with Subcell Resolution*, J. Comput. Phys., **83** (1989), pp. 148-184; also ICASE Report # 87-56

[8] A. Harten, *Discrete Multiresolution Analysis and Generalized Wavelets*, J. Appl. Numer. Math., **12** (1993), pp. 153-192; also UCLA CAM Report 92-08 (1992)

[9] A. Harten, *Multiresolution Representation of Data*, UCLA CAM Report 93-13 (1993)

[10] A. Harten, *Multiresolution Representation of Data II: General Framework*, UCLA CAM Report 94-10 (1994); SIAM J. Numer. Anal. **33** #3 pp 1205-1256 (1996)

[11] A. Harten, *Multiresolution Representation of Cell-Averaged Data*, UCLA CAM Report 94-21 (1994)

[12] A. Harten, B.Engquist, S. Osher and S. Chakravarthy, *Uniformly High Order Accurate Essentially Non-Oscillatory schemes III* . Journal Comput. Phys. (1987) **71** pp 231-303

[13] A. Harten and S. Chakravarthy, *Multi-dimensional ENO Schemes for General Geometries*, ICASE Report 91-76, September 1991; also submitted to J. Comput. Phys.

Appendix I: The Detection Mechanism

We shall describe now the strategy we use to determine whether or not the SR technique should be applied at a given cell. Our mechanism also detects a singularity at a grid point. After wide experimentation, we confirm that our strategy successfully detects δ-type singularities (of $O(1)$ strength as well as those labeled 'small'), jumps and corners in the (discrete) incoming signal.

As mentioned in section 5, we use the fourth and fifth order divided differences to isolate first those cells which exhibit "non-smooth" behavior.

For each $j \geq 1$, define

$$\begin{aligned} dci4(j) &:= \min(|H[j-1,4]|, |H[j-2,4]|, |H[j-3,4]|, |H[j-4,4]|) \\ dce4(j) &:= \min(|H[j-1,4]|, |H[j-2,4]|, |H[j-3,4]|) \\ dni4(j) &:= \max(|H[j,4]|, |H[j-5,4]|) \\ dne4(j) &:= \max(|H[j,4]|, |H[j-4,4]|) \end{aligned}$$

and

$$\begin{aligned} dci5(j) &:= \min(|H[j-1,5]|, |H[j-2,5]|, |H[j-3,5]|, |H[j-4,5]|, |H[j-5,5]|) \\ dce5(j) &:= \min(|H[j-1,5]|, |H[j-2,5]|, |H[j-3,5]|, |H[j-4,5]|) \\ dni5(j) &:= \max(|H[j,5]|, |H[j-6,5]|) \\ dne5(j) &:= \max(|H[j,5]|, |H[j-5,5]|). \end{aligned}$$

If

$$\begin{cases} h^{1/2} dce4(j) > dne4(j) & or \\ h^{1/2} dce5(j) > dne5(j) \end{cases} \tag{74}$$

there is a possible singularity at $\approx x_j$. If

$$\begin{cases} h^{1/2} dci4(j) > dni4(j) & or \\ h^{1/2} dci5(j) > dni5(j) & or \end{cases} \tag{75}$$

there is a possible discontinuity in (x_{j-1}, x_j).

The second step is to use the function $G_j(x)$ and its derivatives to confirm the presence of a singularity.

REMARK .1. *Note that if $a \approx 1$ (singularity at x_{j-1}) we would have $dce4(j) = O(1) < dne4(j)$ and $dce4(j-1) > dne4(j-1)$. Since a can be slightly smaller or larger than 1, if (74) is satisfied the singularity might be at x_j or in (x_{j-1}, x_j) or (x_j, x_{j+1}). We thus need to look for sign changes in G_j and G_{j+1}. The case $a \approx 0$ has to be considered analogously.*

In our numerical experiments we found that the sign change condition leads sometimes to the application of the SR technique in smooth places. Tables 10, 11 and 12 (which are constructed via Taylor expansions) reflect the behavior of the functions $G^{(m)}$ near the three types of singularities we want to identify. Using the information in these tables we add more conditions to the definition of a *singular* cell. All of these conditions are satisfied at the specified singularities. In our numerical experiments we find that they effectively filter out fake singularities.

Our strategy is as follows:

If (74) holds, we check each set of conditions specified below. If (75) holds, we check only the sets (79),(80) and (81). We also check these three sets if (74) holds at $j-1$ (see

	$x_d \in (x_{j-1}, x_j)$		$x_d = x_j$	
z	$G_j(z)$	$G_j'(z)$	$G_j(z)$	$G_j'(z)$
x_{j-1}	$(a-1)h[H']_{x_d}$	$[H']_{x_d}$	$-h[H']_{x_d}$	$[H']_{x_d}$
x_j	$ah[H']_{x_d}$	$[H']_{x_d}$	$O(h^{p+2})$	$[H']_{x_d}$
x_{j+1}	$(a+1)h[H']_{x_d}$	$[H']_{x_d}$	$h[H']_{x_d}$	$[H']_{x_d}$

TABLE 10
δ-type singularity in $f(x)$ ($[H']_{x_d} \neq 0$) .

	$x_d \in (x_{j-1}, x_j)$		$x_d = x_j$	
z	$G_j'(z)$	$G_j''(z)$	$G_j'(z)$	$G_j''(z)$
x_{j-1}	$(a-1)h[H'']_{x_d}$	$[H'']_{x_d}$	$-h[H'']_{x_d}$	$[H'']_{x_d}$
x_j	$ah[H'']_{x_d}$	$[H'']_{x_d}$	$O(h^{p+1})$	$[H'']_{x_d}$
x_{j+1}	$(a+1)h[H'']_{x_d}$	$[H'']_{x_d}$	$h[H'']_{x_d}$	$[H'']_{x_d}$

TABLE 11
jump in $f(x)$ ($[H'']_{x_d} \neq 0$) .

	$x_d \in (x_{j-1}, x_j)$		$x_d = x_j$	
z	$G_j'(z)$	$G_j''(z)$	$G_j'(z)$	$G_j''(z)$
x_{j-1}	$\frac{1}{2}(a-1)^2h^2[H''']_{x_d}$	$(a-1)h[H''']_{x_d}$	$\frac{1}{2}h^2[H''']_{x_d}$	$-h[H''']_{x_d}$
x_j	$\frac{1}{2}a^2h^2[H''']_{x_d}$	$ah[H''']_{x_d}$	$O(h^{p+1})$	$O(h^p)$
x_{j+1}	$\frac{1}{2}(a+1)^2h^2[H''']_{x_d}$	$(a+1)h[H''']_{x_d}$	$\frac{1}{2}h^2[H''']_{x_d}$	$h[H''']_{x_d}$

TABLE 12
corner in $f(x)$ ($[H'']_{x_d} \neq 0$).

remark .1). As soon as one of the conditions in a particular set fails, we reject the outcome of that set and go to the next set. If none of the sets gives a positive outcome, the cell is left un-flagged.

$$\left.\begin{array}{l} G_j'(x_{j+1})G_j'(x_{j-1}) \leq 0 \\ |G_j'(x_j)| \leq h\min(|G_j'(x_{j-1})|, |G_j'(x_{j+1})|) \\ 0 \leq \min(G_j''(x_{j-1})G_j''(x_j), G_j''(x_{j+1})G_j''(x_j)) \\ |G_j'(x_{j+1})| < |G_j''(x_{j+1})| \\ |G_j'(x_{j-1})| < |G_j''(x_{j-1})| \end{array}\right\} \underline{\text{jump at } x_j} \tag{76}$$

$$\left.\begin{array}{l} G_j''(x_{j+1})G_j''(x_{j-1}) \leq 0 \\ |G_j''(x_j)| \leq \min(|G_j''(x_{j-1})|, |G_j''(x_{j+1})|)h^{\frac{1}{2}} \\ G_j'(x_{j+1}) * G_j'(x_{j-1}) \geq 0 \\ |G_j'(x_{j+1})| < |G_j''(x_{j+1})| \\ |G_j'(x_{j-1})| < |G_j''(x_{j-1})| \end{array}\right\} \underline{\text{corner at } x_j} \tag{77}$$

$$\left.\begin{array}{l} G_j(x_{j+1})G_j(x_{j-1}) \leq 0 \\ |G_j(x_j)| \leq h\min(|G_j(x_{j-1})|, |G_j(x_{j+1})|)/ave \\ 0 \leq \min(G_j'(x_{j-1})G_j'(x_j), G_j'(x_{j+1})G_j'(x_j)) \\ |G_j(x_{j+1})| < |G_j'(x_{j+1})| \\ |G_j(x_{j-1})| < |G_j'(x_{j-1})| \end{array}\right\} \underline{\text{delta at } x_j} \tag{78}$$

where $ave := (|G'(x_{j-1})| + |G'(x_j)| + |G'(x_{j+1})|)/3$.

$$(79)\qquad \left.\begin{array}{l} G_j'(x_j)G_j'(x_{j-1}) < 0 \\ \min(|G_j'(x_{j-1})|, |G_j'(x_j)|) > h^2 \\ 0 \le \min(G_j''(x_{j-1})G_j''(x_j), G_j''(x_{j+1})G_j''(x_j)) \\ |G_j'(x_j)| < |G_j''(x_j)| \\ |G_j'(x_{j-1})| < |G_j''(x_{j-1})| \end{array}\right\} \underline{\text{jump in } (x_{j-1}, x_j)}$$

$$(80)\qquad \left.\begin{array}{l} G_j''(x_j)G_j''(x_{j-1}) < 0 \\ \min(|G_j''(x_{j-1})|, |G_j''(x_j)|) > h^2 \\ 0 \le \min(G_j'(x_{j-1})G_j'(x_j), G_j'(x_{j+1})G_j'(x_j)) \\ |G_j'(x_j)| < |G_j''(x_j)| \\ |G_j'(x_{j-1})| < |G_j''(x_{j-1})| \end{array}\right\} \underline{\text{corner in } (x_{j-1}, x_j)}$$

$$(81)\qquad \left.\begin{array}{l} G_j(x_{j+1})G_j(x_j) < 0 \\ \min(|G_j(x_{j-1})|, |G_j(x_{j+1})|) > h^2 ave \\ 0 \le \min(G_j'(x_{j-1})G_j'(x_j), G_j'(x_{j+1})G_j'(x_j)) \\ |G_j(x_j)| < |G_j'(x_j)| \\ |G_j(x_{j-1})| < |G_j'(x_{j-1})| \end{array}\right\} \underline{\text{delta in } (x_{j-1}, x_j)}$$

REMARK .2. *We have seen in section 4 that $G_j(x)$ can be expressed directly in terms of the sampled data $\mathcal{D}f$. Thus, these conditions can be checked without explicit knowledge of $\tilde{\mathcal{D}}H$. We must note that the derivation of G_j in terms of $\mathcal{D}f$ explicitly assumes that $\mathcal{S}_{j-1} \cap \mathcal{S}_{j+1} = \emptyset$. Regardless of the outcome of Algorithm I for these two stencils, when using G_j to confirm the presence of a singularity we always (as we should) use stencils that do not cross the singularity.*

REMARK .3. *The use of 'ave' in (78) and (81) helps in localizing "small" deltas. The size of the jumps and corners is assumed to be $O(1)$.*

If a singularity is confirmed at a particular location, we proceed as follows:

If the singularity is located in (x_{j-1}, x_j) we apply the SR technique. We must also check the stencils in the neighboring polynomial pieces to make sure that the accuracy is maintained (they do not cross the singularity). We should then have

$$i(j-1) = j - r - 1, \qquad i(j+1) = j + 1$$

and we use Algorithm II to determine $\mathcal{S}_{j-2}$ and $\mathcal{S}_{j+2}$. It can be proven (using Taylor expansions) that the stencils obtained with Algorithm I for intervals further away from the singularity, do not cross it, i.e $i(j+n) \ge j+1$ and $i(j-n) \le j-r+1$ for $n = 3, 4, \ldots$ as long as we are far enough from other singularities.

If the singularity is located at the grid point x_j it is sufficient to modify the neighboring stencils (no SR is needed). We take

$$i(j) = j - r, \qquad i(j+1) = j + 1$$

and use Algorithm II to determine $i(j-1)$ and $i(j+2)$. It can also be proven that $\mathcal{S}_{j+n}$ and $\mathcal{S}_{j-n+1}$ do not cross the singularity for $n \ge 3$, as long as we are far enough from other singularities.